Spring 2021

Pyridinediimine Complexes with Coordination Sphere Interactions Relevant to Copper and Non-Heme Iron Enzymes

Pui Man Audrey Cheung
Western Washington University, aomshis@gmail.com

Recommended Citation

Cheung, Pui Man Audrey, "Pyridinediimine Complexes with Coordination Sphere Interactions Relevant to Copper and Non-Heme Iron Enzymes" (2021). *WWU Graduate School Collection*. 1039.
https://cedar.wwu.edu/wwuet/1039

Pyridinediimine Complexes with Coordination Sphere Interactions Relevant to Copper and Non-Heme Iron Enzymes

By

Pui Man Audrey Cheung

Accepted in Partial Completion
of the Requirements for the Degree
Master of Chemistry

ADVISORY COMMITTEE

Chair, Dr. John D. Gilbertson

Dr. Margaret L. Scheuermann

Dr. Tim Kowalczyk

GRADUATE SCHOOL

Dr. David L. Patrick, Dean

MASTER'S THESIS

Pui Man Audrey Cheung

May 4, 2021

Pyridinediimine Complexes with Coordination Sphere Interactions Relevant to Copper and Non-Heme Iron Enzymes

A Thesis

Presented to

The Faculty of

Western Washington University

In Partial Fulfillment

Of the Requirements for the Degree

Master of Chemistry

by

Pui Man Audrey Cheung

May 2021

Abstract

Primary and secondary coordination sphere interactions with proximal Brønsted-Lowry acid/base sites were investigated using a family of pyridinediimine (PDI) complexes. The PDI ligands used in this project could be easily prepared by the Schiff base reactions with commercially available diamines as proton relays. Upon activation, the pendant Brønsted site and accessible electrons were arranged in a single scaffold that allowed the transportation of both protons and electrons to occur.

Two new PDI complexes with morpholine (**6**) and pyrrolidine (**7**) derivatives were introduced to the pendant PDI family. The proton dissociation constant of **6**Fe(CO)$_2$ and **7**Fe(CO)$_2$ were measured [pK_a (CD_3CN) = 17.1 and 18.3, respectively]. The PDI complexes were subjected to reactions with nitrite and monitored via UV-Vis and IR spectroscopy, in which they exhibited much faster initial rates than some of the previously reported pendant PDI complexes. The rate enhancement effect was clearly evidenced by the stability of the corresponding mononitrosyl iron complex (MNIC) intermediate. These results had not yet been observed in other mononuclear PDI complexes and was attributed to the unique combination of proton responsivity, redox-activity and hemilability in **6** and **7**.

Acknowledgments

I thank the Thesis Committee, Chair Dr. John Gilbertson, Dr. Margaret Scheuermann and Dr. Tim Kowalczyk for their time and effort in editing this thesis document. I am especially grateful to Dr. John Gilbertson for his advice and mentorship in the last few years, and to Dr. Margaret Scheuermann for sharing useful tips for graduate school. It ended up taking a long time for me to feel ready to finish up this thesis, and I cannot express my gratitude enough to the Thesis Committee for continuing to support my thesis completion after all these years.

Research Advisor:	Dr. John D. Gilbertson	
Thesis Committee:	Dr. Margaret L. Scheuermann	
	Dr. Tim Kowalczyk	
Research Group Members:	Walker Marks	Wyatt Parks
	Doug Baumgardner	Kris Aguayo
Former Group Members:	Kyle Burns	Mayra Delgado
	Josh Ziegler	Jade Porubek
	Yubin Kwon	Tori Quade
Instrument Technicians:	Dr. Hla Win-Piazza	
	Sam Danforth	
Mossbauer:	Dr. Takele Seda	
X-ray Crystallographer:	Dr. Lev Zakharov (University of Oregon)	
EPR:	Victoria Oswald (University of California)	
Support:	Most of the research projects were supported by funding from NIH, NSF and also ACS PRF.	

Table of Contents **Page**

List of Figures and Schemes

List of Tables and Equations

List of Supporting Information Figures

List of Abbreviations

Å	Angstrom
CH_3CN	Acetonitrile
Atm	Atmosphere
bz15c5	Benzo-15-crown-5 ether
15c5	15-crown-5 ether
BPDI	(di)Benzoylpyridinediimine
CV	Cyclic Voltammogram
DCM	Dichloromethane
DNIC	Dinitrosyl Iron Complex
e^-	Electron
EPR	Electron Paramagnetic Resonance
ET	Electron Transfer
E-F	Enemark-Feltham
EtOH	Ethanol
Fc	Ferrocene
FT-IR	Fourier Transform Infrared
δ	Isomer shift
MeCN	Acetonitrile
MeOH	Methanol
MNIC	Mononitrosyl Iron Complex
NiR	Nitrite reductase
NHE	Normal hydrogen electrode
NMR	Nuclear Magnetic Resonance
ORTEP	Oak Ridge Thermal Ellipsoid Plot
OCP	Open circuit potential
ppm	parts per million
H^+	Proton
PCET	Proton-coupled electron transfer
PDI	Pyridinediimine
ΔE_Q	Quadrupole Splitting
THF	Tetrahydrofuran
NEt_3	Triethylamine
UV-Vis	Ultraviolet-Visable

Chapter 1 – Introduction

1.0 Chemical Activation in Biology

The biogeochemical cycle encompasses a diversity of pathways ranging from the metabolism of small molecules such as CO_2, NO_2^-, O_2, to the biosynthesis of complex molecules.[1–4] From photosynthesis to respiration, almost all the important chemical transformations in biology are mediated by metalloenzymes found in microorganisms and plants.[1]

One of the most exemplified biological processes of interest is the nitrogen cycle. Unsurprisingly, a major portion of naturally occurring nitrogen exists as inorganic nitrogen species, either in the most inert form, N_2, or in a highly oxidized form, NO_3^-.[5–7] These readily available nitrogen sources are however often toxic or unsuitable for biosynthetic purposes. The required transformation takes place in the nitrogen cycle via the activation of inorganic nitrogen mediated by various metalloenzymes classified by their native functions. The reductive processes of generating NH_3 or glutamine are accomplished by nitrogenases. Nitrate reductases (NaRs) and nitrite reductases (NiRs) are responsible for nitrogen fixation, nitrogen assimilation and denitrification, respectively. Concomitantly, the nitrogen cycle turns over as the oxidative processes occurs, countering the production of reduced nitrogen. Other assimilatory processes mediated by NiRs and NO reductases (NORs) in bacteria and fungi produce N_2O from NO_2^- and NO.[7] All of these transformations occur in ambient conditions. On the other hand, chemical transformation of small molecules in a laboratory setting tends to be thermodynamically challenging and often requires harsh reaction condition to elevate overpotential.[8,9] The difficulty to industrially derive energy from small molecules can exemplified by the Nobel-winning Haber-Bosch process, which accounts for the global production of NH_3 from atmospheric N_2.[7] The process poses a tremendous energy footprint due to the excessive consumption of H_2 gas as the reducing agent under high temperature and high pressure conditions,[10] contrary to the biological transformation of N_2 to NH_3/NH_4^+, which requires energy via ATP hydrolysis.[6,11] Unlike the 6-electron Haber-Bosch process, the nitrogenase-mediated process takes place in the presence of both protons and electrons under ambient conditions and also produces H_2 as a by-product. In the well-examined FeMoco containing nitrogenases,[12,13] eight electrons are involved. Two out of eight electrons are consumed to form one equivalent of H_2 per N_2 activated. The reduced activation energy in nitrogenase is ascribed to a combination of ligand and/or active site interactions that facilitate the binding to MgATP and electron transfer.[14,15]

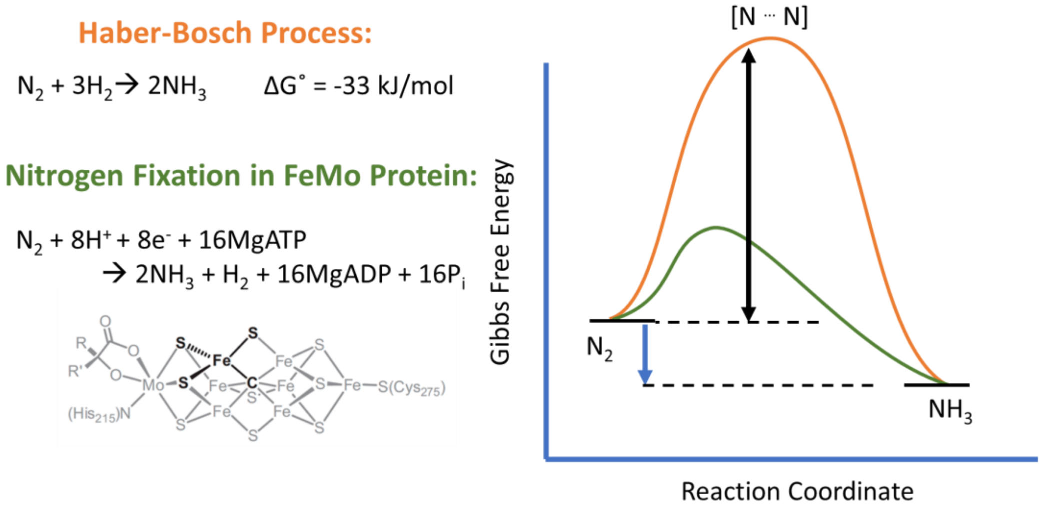

Figure 1.1 Haber-Bosch process vs nitrogen fixation mediated by nitrogenase.

In the assimilatory pathway of the nitrogen cycle, nitrite reduction is mediated by either cytochrome cd_1 or multicopper NiRs.[6] Although the NiR family consists of a relatively limited variation of active sites—comparing to other metalloenzymes, these systems are ubiquitous and representative of other active sites in nature. In the context of molecular catalysis, the structural effect is ascribed to the primary and secondary coordination sphere configuration. In order to gain better understanding in how biology handles the cost of activation energy, the coordination and reactivity in these metalloenzymes will be explored.

1.1 Active Site with Iron

The most common NiRs are cytochrome related metalloenzymes, which are classified based on the heme-iron cofactor presented in these proteins.[16] In fact, the iron-porphyrin moiety is an extremely common motif in biology. Porphyrin rings with modifications allow the hemeproteins to cover a wide spectrum of functionalities, ranging from the transferring of electrons to the scavenging, sensing and/or transportation[17–20] of other small molecules (Figure 1.2). Low molecular weight proteins containing these hemes are known as cytochromes, and they are the key cofactors and participants in a variety of biological processes.

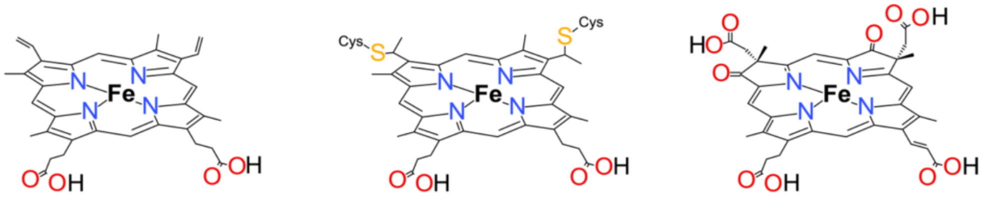

Heme *b*
Hemoglobin, myoglobin

Heme *c*
Cytochrome *c* oxidase

Heme d_1
Cytochrome cd_1 nitrite reductase

Figure 1.2 Common heme structures and examples of hosting proteins. This figure was adapted from literature.[6]

How are heme irons so ubiquitous? One consideration is the $Fe^{II/III}$ reduction potentials of the cytochrome family, which span about from -475 mV to +450 mV vs NHE,[16] in the range necessary for those biological processes.[21] Remarkably, modulation of the redox properties of $1Fe^{II/III}$ through the secondary coordination sphere can be just as effective as tuning via the primary sphere.[22,23] Attributed to the electrostatic interactions, proximal side chains with positive charges or hydrogen bonding can lead to an anodic shift of $Fe^{II/III}$, and inversely, negatively charged residues in proximity can lead to a cathodic shift.[16] All of these modifications can also affect the liability and substrate binding/releasing.

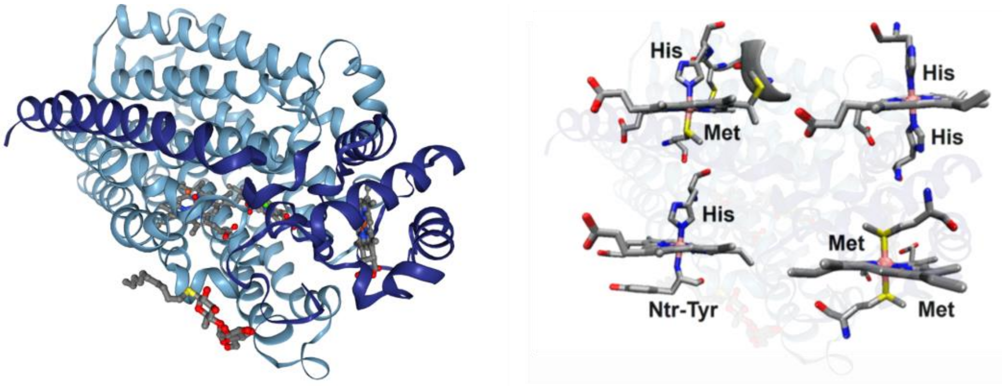

Figure 1.3 Cytochrome cd1 from Pseudomonas aeruginosa. Some of the variations in axial ligands were shown (PDI ID: 5GUW)[24].

Similar redox tuning properties has been reported in most synthetic complexes, where a wide range of $Fe^{II/III}$ redox potentials have become accessible.[25] In complexes incoporated with proximal Lewis acids (Figure 1.4, **A** – **D**, $\Delta E_{1/2}$ values represent the difference in metal-based reduction potentials before and after encapsulation), the metal-based reduction potentials are typically shifted anodically upon the encapsulation of a redox inactive alkai ion.[26–28] On the other hand, with a redox-active ligand scaffold such as the pyridinediimine (PDI) family, accessible energy should be evaluated by the ligand-based reduction potentials.[29–31] In the recently reported PDI systems $Fe(^{15c5}PDI)(CO)_2$ (15c5 = 15-crown-5 ether) and $Fe(^{15bz5}PDI)(CO)_2$ (15bz5 = benzo-15-crown-5 ether), only 31 and 50 mV anodic shift were resulted, respectively, upon the encapsulation of redox inactive metal such as Na^+ (Figure 1.4, **E** and **F**, $\Delta E_{1/2}$ values represent the difference in ligand-based reduction potentials).[32,33]

Figure 1.4 Redox potential coupled to proximal Lewis acids. Chemdraw of (**A**) crown ether appended ferrocene,[34] (**B**) crown ether incorporated Co(salen),[35] (**C**) bimetallic metalloligand system[36,37] and (**D**) manganese cubane core structure[27,38,39] (M^{n+} = alkai metal ion). (**E**) and (**F**) are PDI complexes $Fe(^{15c5}PDI)(CO)_2$ and $Fe(^{15bz5}PDI)(CO)_2$.

Considerable change in redox potential has been also reported in model systems incorporated H-bonding network in the secondary coordination sphere.[40–42] The reduction potentials are shifted anodically upon the protonation of the Brønsted base bearing secondary sphere (Figure 1.5, **A** – **C,** $\Delta E_{1/2}$ values represent the difference in metal-based reduction potentials before and after protonation).[8,43,44] Similar to the uncoupling effect in the $Fe(^{15bz5}PDI)(CO)_2$ systems, the anodic shifting is minimized in the pendant Bronted base incorporated PDI family upon protonation (Figure 1.5, **D** and **E**, $\Delta E_{1/2}$ values represent the difference in ligand-based reduction potentials).[45]

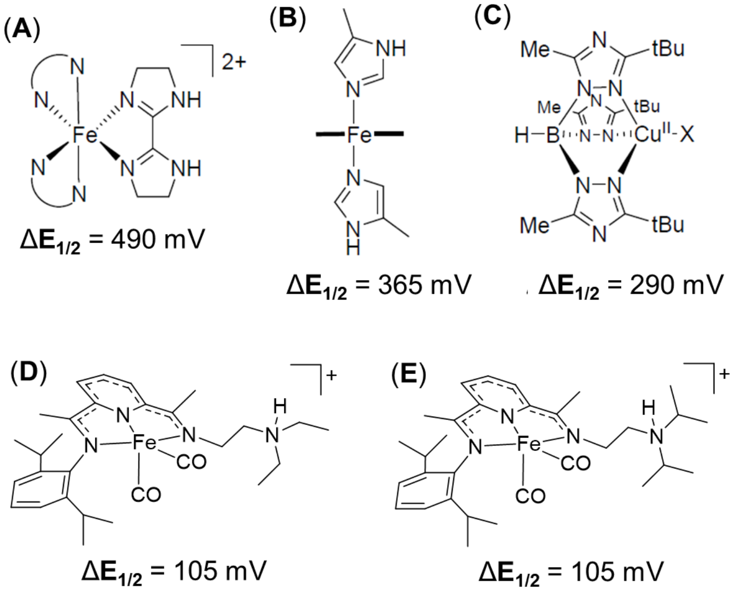

Figure 1.5 Redox potential coupled to proximal Brønsted acid/base. Chemdraw of protonated (**A**) Fe^{II}(tris(2,2'bisimdazoline)$^{2+}$,[43,46] (**B**) [(TPP)Fe^{II}(ImH)$_2$] (TPP = tetraphenylporphyrin; ImH = 4-methylimidazole),[47] (**C**) Ttz$^{t\text{-}Bu,Me}$CuCl (Ttz = [tris(triazolyl)borate]),[48] 63(**D**) and (**E**) are PDI complexes Fe(^{DEA}PDI)(CO)$_2$ and Fe(didpa)(CO)$_2$ (DEA = diisopropylamine; didpa = [(2,6-^{i}PrC$_6$H$_3$)(N=CMe)(N(iPr)$_2$C$_2$H$_4$)(N=CMe)C$_5$H$_3$N]).[49,50]

1.2 **Copper Active Site**

Apart from the Fe-type NiR, the genetically unrelated Cu-NiR family accounts for a third of the denitrifying reactions in nature. Both Type 1 and Type 2 copper active sites have been found in Cu-NiR. The T1 copper delivers electrons over a distance of 13 Å to the T2 site where the bound NO_2^- is subsequently reduced.[51]

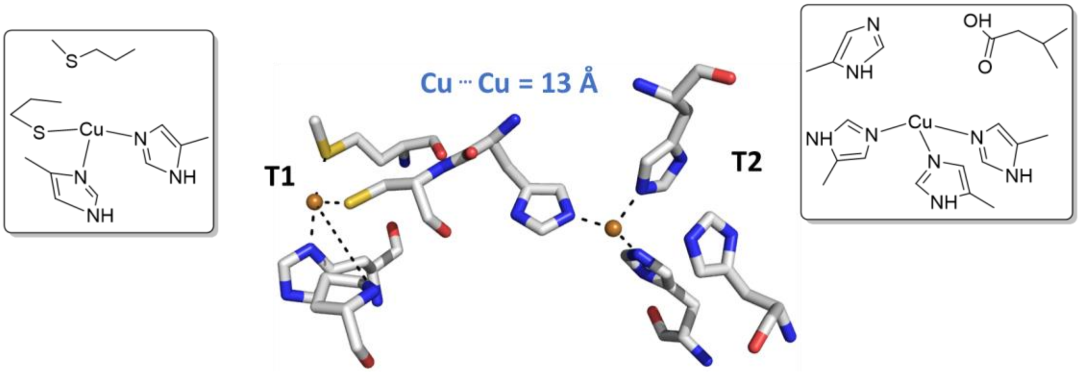

Figure 1.6 Dicopper nitrite reductase (Cu-NiR). Monomeric T1 and T2 copper centers within the same subunit of *Achromobacter cycloclastes* Cu-NiR (PDB ID: 1NIA).[52] ChemDraw representations of the T1 (left) and T2 (right) site are shown.

Copper active sites have been found in well-conserved coordination spheres in different enzymes. The types of copper centers are classified by their ligand environment, geometry and spectroscopic properties. The most prominent copper sites are the T1 family as they are ubiquitous electron transporters. T1 copper center has a characteristic 2N1S trigonal planar base stabilized by two histidine and one cysteine, and a weak axial coordination to methionine. The geometric configuration is in fact not favorable for the biological active form of Cu^{2+} but slightly favorable for the reciprocate Cu^+. The constraint imposed by the active site ligands is known as the entatic state,[53,54] which serves as a rack that configures the Cu^{2+} center in a position that minimizes the internal reorganization energy (λ_{int}) for the formation of Cu^+. The effect due to reorganization described in the semiclassical Marcus equation is pronounced, as the lowered overall λ is directly proportional to the increase of k_{ET}.[21]

In my undergraduate research, some copper complexes have been made using the pyridindiimine ligands with structural constrain that resemble the entatic state in copper proteins. The rate constant of electron transfer was initially studied via the NMR line broadening experiments plotting Cu^{2+} concentrations vs the-width-at-half-maximum of a chosen resonance. Nevertheless, the project was obstructed as the disproportionation of Cu^{+} into Cu^{2+} and Cu^{0} occurred readily at room temperature even though the PDI ligand was supposed to stabilize these Cu complexes. The spontaneous formation of two other paramagnetic species resulted in much broader NMR baseline, making any line broadening data insignificant comparing to the baseline concentration. This was improved slightly when the NMR experiments were repeated at lowered temperatures, although a cryogenic temperature might be required to eliminate any interference due to disproportionation reactions. The currently available NMR instrument is, however, not optimized for frozen NMR sample. Therefore, alternative methods of measuring ET rate would be necessary to iterate our data.

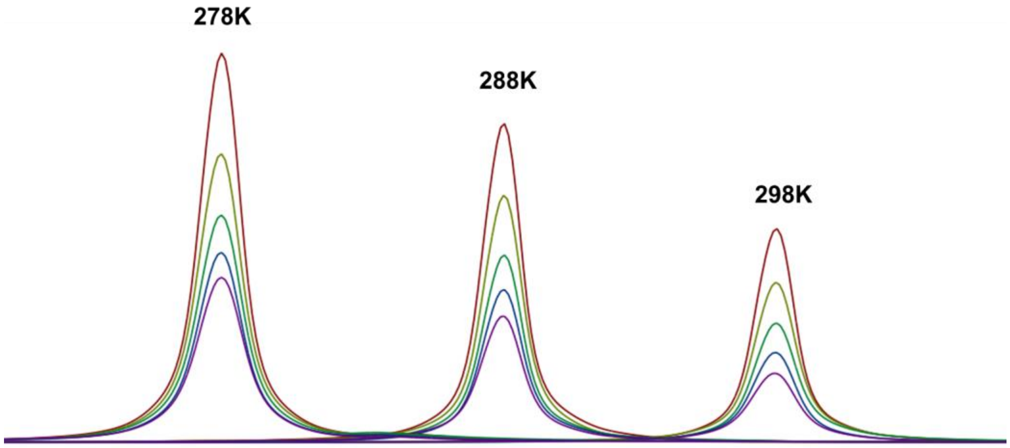

Figure 1.7 NMR line broadening experiments at 278K, 288K and 298K. The broadening are relatively small comparing to the width of the baseline (purple line, [Cu^{2+}] = 0 mM) due to disproportionation, which was only slightly improved at 278K.

1.3 Research Objectives

Using the synthetic models, some typical structural features implicated by Fe- and Cu-NiRs were examined, such as the coordination environment that influences ET rate, ligand binding, rate determining step and other kinetic parameters favoring substrate activation. One of these effects has been explored in my undergraduate research involving the Cu(PDI) complexes. For our ongoing interest in small molecule activation, we continued to use PDI as a platform to incorporate biological relevant features in metalloenzymes. Specifically, the coordination sphere interactions allowing rapid transfer of both protons and electrons are revisited. With the available instrumentation in hand, a family of Fe(PDI) complexes integrating proton responsivity were synthesized and characterized.

Chapter 2 – Synthesis and Characterization of PDI Complexes.

2.0 Synthesis of Symmetric PDI Ligands

First due to the development of using Fe- and Co-PDI catalysts in olefin polymerization,[55–59] a variety of pyridinediimine (PDI) ligands have been reported with detailed experimental procedures and characterization.[60–64] The PDI scaffolds were chosen to modulate bioinspired catalysts due to their versatile redox-activity given that they can store electrons in the metal-ligand cooperative conjugation.[61,62,65,66,64] In the synthetic perspective, PDI ligands are highly accessible and tunable. The reaction conditions and chemicals required for the Schiff-base condensation are typically safe to handle.

Symmetric ligands **1** – **3** in Scheme 2.1 are generally formed via the acid-catalyzed condensation of commercially available 2,6-diacetylpyridine with the corresponding ortho-substituted aniline. The reaction can be easily driven to completion by the removal of water being generated as a by-product.

Scheme 2.1 Generic synthesis of symmetric PDI ligands.

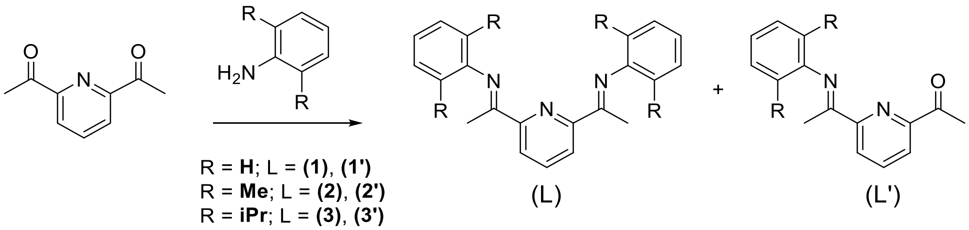

In our hands, symmetric bis-ligands (2,6-(2,6-$R_2C_6H_3N$=CMe)$_2C_5H_3N$) **1** – **3** were synthesized using a Dean-Stark apparatus, in which a mixture of 2,6-diacetylpyridine, excess of aniline (**1**: aniline, **2**: 2,6-dimethylaniline or **3**: 2,6-diisopropylaniline) and a catalytic amount of ptoluenesulfonic acid (p-TSA or TsOH) in toluene was allowed to reflux at 84°C for 12 – 36 hours. Due to the water-toluene azeotrope, the by-product water evaporated below its normal boiling point and condensed in the Dean-Stark trap. The utilization of the Dean-Stark apparatus effectively drives the reaction to completion.

Depending on the stability of the aniline derivatives, the reaction in Scheme 2.1 often resulted in a mixture of the bis- and mono-substituted imines. One way to purify the desired product is flashing through a neutral alumina column with a solvent mixture such as hexane/EtOAc. Alternatively, the desired product can be purified when a suitable solvent for washing or re-crystallization is identified. For example, **1** and **2** can be re-crystallized in dry ethanol and methanol, respectively, while leaving **1’** and **2’** in solution. On the other hand, the purification of **3** can be simply achieved by washing the crude solid with acetone due to the fact that **3** is insoluble in most polar solvents, including acetone.

A series of symmetric dibenzoylpyridinediimine (BPDI) ligands analogous to **2** and **3** were also synthesized and characterized (Scheme 2.2). The synthesis procedure of BPDI **4** and **5** is the same as **1 – 3**, followed by a flash column with silica ($CHCl_3$/pentane/Et_3N) or simply a MeOH wash to purify the bis-imines. The ^1H NMR spectrum is in agreement with the reported data in literature.[59,67,68]

Scheme 2.2 Generic synthesis of symmetric BPDI ligands; mono-substituted products are omitted.

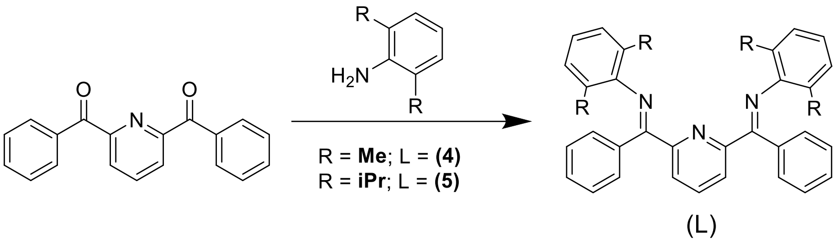

2.1 Remarks of Steric and Chelating Effect

Using the symmetric PDI and BPDI ligands, the synthesis of monomeric square planar (SP) Cu^I compounds becomes accessible. Although unusual for the d^{10} configuration, these ligands impose a geometric constraint on the Cu^I center similar to the *entatic* state in the biological copper centers introduced above. In T1 copper active sites, the $Cu^{I/II}$ center is forced to reside in the NNS trigonal planar with an axial S atom from methionine. The 2N2S pocket chelates the $Cu^{I/II}$ center in a *rack* that is "uncomfortable" for Cu^{II} but slightly preferable for Cu^I. This configuration ultimately reduces the reorganization energy required for the geometric rearrangement between $Cu^{I/II}$ occurs during ET.[69–72,53] Unlike those in nature, the rack state in Cu(PDI) system is inversed—it is the Cu^I center that adapted the "uncomfortable" configuration, which favors the reorganization from Cu^I to Cu^{II} in the synthetic model. X-ray crystallographic data revealed that the monomeric Cu^I(PDI) family were distorted square planar,[73] quantified by the τ_4 parameter derived from the sum of the two largest angles in the copper center divided by 141˚, with 0 being a perfect square planar and 1 being a perfect tetrahedral.[74]

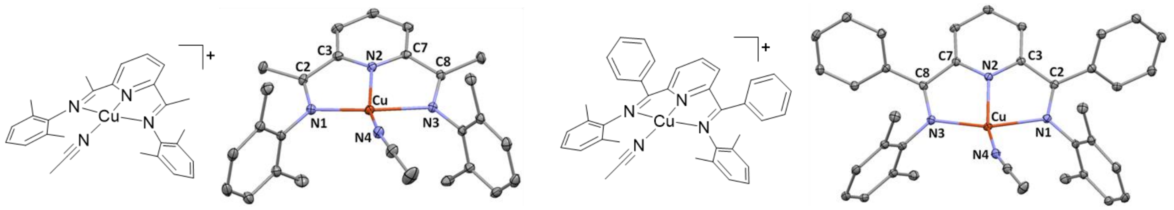

Figure 2.1 Examples of monomeric CuI(PDI) complexes. ORTEP and Chemdraw of $[2Cu^{I}(CH_3CN)][PF_6]$ and $[4Cu^{I}(CH_3CN)][PF_6]$. Counter ions are omitted for clarity.

2.2 Synthesis of Asymmetric Pyridinediimine Scaffolds

To further explore the realm of biocatalysis modeling, the mono-substituted iminopyridine was utilized to install chemical derivatives of functional residues in metalloenzymes. Two PDI systems incorporated with neutral base derivatives, ^{Mor}PDI (**6**) and ^{Pyrr}PDI (**7**) (Mor = morpholine; Pyrr = pyrrolidine) have been synthesized and characterized.

Scheme 2.3 Condensation reaction with proton responsive diamines and subsequent protonation.[75,76] The pK_a values in CD_3CN of conjugated acids of morpholine, pyrrolidine and diisopropylamine are shown in blue.

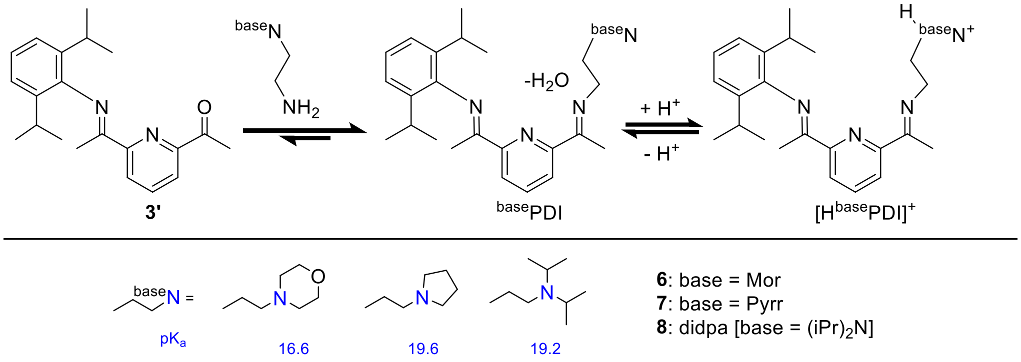

The procedure of making didpa (**8**) has been adapted for the preparation of **7**, which involved a 36-hour-incubation of a sealed pressure vial containing **3’** and a large excess of the diamine (Scheme 2.3). After an overnight freeze precipitation in MeOH or MeCN, **7** was isolated in decent yield (72%). The unreacted diamine was most likely not recoverable after the long exposure to heat. On the other hand, attempts to synthesize **6** using the same method were unsuccessful.

Depending on the reaction mixture and the pK_a of the pendant amine, residual water may further react with the product non-catalytically as an acid. Furthermore, the properties of diamines can dramatically affect the solubility, and consequently the yield and purity of ^{base}PDI. The base-catalyzed method tends to be synthetically more compatible with the ^{base}PDI with a more basic pendant amine. The pK_a values (in CD_3CN) of the base analogues of **7** (pyrrolidine, 19.6) and **8** (diisopropylamine, 19.2) are very similar, whereas the pendant base analogue of **6** (morpholine, 16.6) is considerably more acidic.

The Dean-Stark method was also attempted to synthesize ^{base}PDI (**6** – **8**). Under the condition analogous to the synthesis of **1** – **5**, a mixture containing **3’** and the starting diamines ($^{base}NC_2H_4NH_2$) for ^{base}PDI quickly turned into dark brown when treated with toluene and catalytic TsOH. The precipitation of a water-soluble white salt occurred as the brown mixture cooled back to room temperature. The ^1H NMR of the white precipitate isolated from the Dean-Stark mixture intended for **7** reveal that it is either a decomposition product of toluene or 2,6-diisopropylaniline (Figure S2).

Scheme 2.4 Metal-templated condensation of **6**.

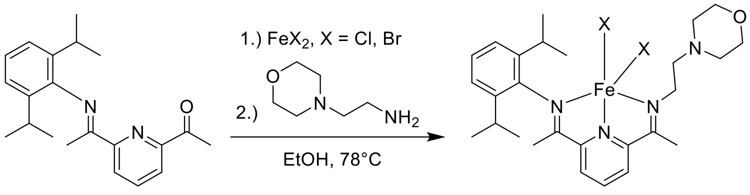

3'

6FeX2

The scaffold of **6** has been shown accessible via a metal-templated Schiff base synthesis. Under a flow of N_2, a solution containing the $^{\mathrm{Mor}}NC_2H_4NH_2$ was added to a warm suspension of **3'** and FeX_2 (X = Cl^- or Br^-) in EtOH and allowed to reflux overnight. The one-pot synthesis shown in Scheme 2.4 generated **6**FeX_2 directly. Unlike **6**FeX_2, the metal-templated synthesis of **7**FeX_2 or **8**FeX_2 in EtOH yielded a sticky purple mixture ascribed to the protonation in the pendant base. Analogous to the previously reported **8**FeX_2, spectroscopically pure **7**$FeCl_2$ can be obtained by simply mixing the pure ligand and $FeCl_2$ in solution and crystallized in MeOH/Et_2O layer diffusion.

Chapter 3 – Redox Property in Multifunctional Pyridinediimine

3.0 Ligand-based electron reservoir

As introduced in Chapter 2, the PDI backbone was chosen to be our modeling platform due to the ability of electron storage and the resulting coordination scaffold with accessible redox states. The redox non-innocent neutral PDI^0 can undergo various reductions to obtain up to three electrons, spanning the formal electronic configurations of PDI^0, $[PDI]^-$, $[PDI]^{2-}$ and $[PDI]^{3-}$ that allow the lower-oxidation states to be chemically accessible when coordinated to a metal and even main group atoms. Extensive spectroscopic and computational studies have revealed multireference characters **3**$Fe(CO)_2$ (**3** = ^{iPr}PDI) arising from a mixed oxidation states of Fe(PDI) unit. For simplicity, the PDI ligand are shown in either the neutral or the reduced formed (Figure 3.1). The dash lines represent the ambiguous oxidation states in $[PDI]^{n-}$ (n = 1, 2 and 3) and the delocalized electron(s).

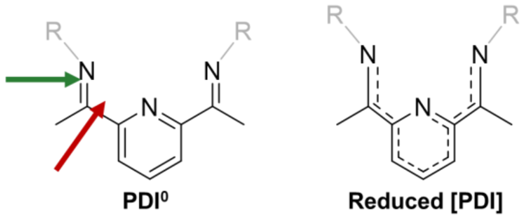

PDI^0 **Reduced [PDI]**

# of e^-	C_{imine} –N_{imine}	C_{imin} –C_{ipso}
0	1.28	1.50
1	1.32	1.44
2	1.36	1.40
3	1.40	1.37

Figure 3.1 Electronic structure of PDI ligand and corresponding bond lengths. Chemdraw representations of electronic structures of PDI^0 and the collective structure of singly and doubly reduced $[PDI]^{n-}$ (n = 1 and 2). The C_{imine}-N_{imine} (green arrow) and C_{imine}-C_{ipso} (red arrow) bond lengths in $[PDI]^n$, (n = 0, 1, 2 and 3) are listed in the table adapted from literature.[77]

3.1 Synthesis and Characterization of Fe(PDI)(CO)$_2$

Scheme 3.1 Two-electron reduction of (^{base}PDI)FeX$_2$.

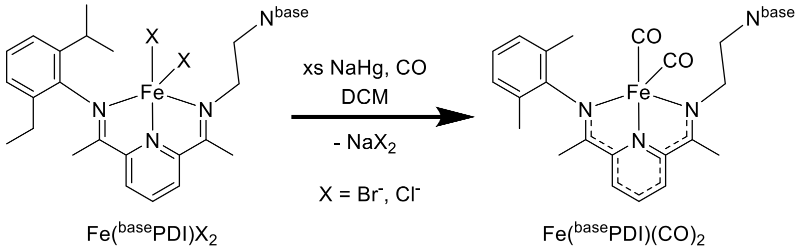

Dianionic PDI can be accessed via the chemically stable form of Fe(PDI)(CO)$_2$. To generate the two-electron-reduced species, the five coordinate high-spin Fe(PDI)X$_2$ complexes (S = 2) were treated with excess NaHg under a CO pressure (Scheme 3.1).[55,65,78,79] The reduction of Fe(^{base}PDI)X$_2$ resulted in Fe(^{base}PDI)(CO)$_2$ with the diagnostic vCO frequencies of 1934 and 1871 cm^{-1} for **6**Fe(CO)$_2$ and 1942 and 1876 cm^{-1} for **7**Fe(CO)$_2$ (Figure S5).

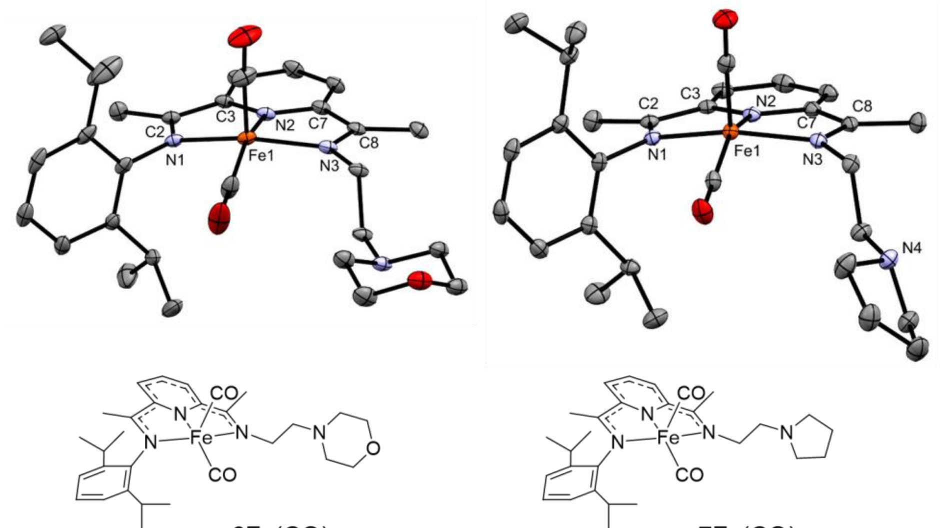

6Fe(CO)$_2$ **7**Fe(CO)$_2$

Figure 3.2 Solid-state structures of **6**Fe(CO)$_2$ and **7**Fe(CO)$_2$. rendered at 30% probability (**6** = ^{Mor}PDI and **7** = ^{Pyrr}PDI). The H atoms have been omitted for clarity. **6**Fe(CO)$_2$: C$_{imine}$-N$_{imine}$ bond lengths = 1.332(2) and 1.324(2) Å; C$_{imine}$-C$_{ipso}$ bond lengths = 1.423(2) and 1.434(2) Å. Selected bond angles (°): ∠OC—Fe—CO 97.62(9), ∠N(2)—Fe(1)—CO 156.22(7), ∠N(1)— Fe(1)—N(3) 153.42(5). **7**Fe(CO)$_2$: C$_{imine}$-N$_{imine}$ bond lengths = 1.332(2) and 1.324(2) Å; C_{imine}-C_{ipso} bond lengths = 1.426(2) and 1.438(2) Å. Selected bond angles (°): ∠OC—Fe—CO 95.65(7), ∠N(2)—Fe(1)—CO 153.81(7), ∠N(1)—Fe(1)—N(3) 154.16(6).

X-ray diffraction data of **6**Fe$(CO)_2$ and **7**Fe$(CO)_2$ elucidated square pyramidal solid state structures (τ_5 = 0.05 in **6** and 0.01 in **7**).[80] The PDI C_{imine}-N_{imine} and C_{imine}-C_{ipso} bond lengths were in the range diagnostic of reduced PDI. The room temperature zero-field Mossbauer spectra yielded δ = -0.08(1), ΔE_Q = 1.46(2) mm/s in **6**Fe$(CO)_2$ and δ = -0.089(3), ΔE_Q = 1.197(3) mm/s in **7**Fe$(CO)_2$, indicative of the S = 0 configurations similar to the previously reported complexes.

As expected, **6**Fe$(CO)_2$ and **7**Fe$(CO)_2$ were both diamagnetic and afforded clean ^{1}H and ^{13}C NMR spectra (Figure S6-7). This allowed the direct measurement of pK_a values based on the ^{1}H NMR chemical shifts of $[^{Mor}NH]^+$ in **6**Fe$(CO)_2$ and $[^{Pyrr}NH]^+$ in **7**Fe$(CO)_2$ according to literature procedures.[50,81] For **6**, $[HEt_3N][BPh_4]$ (pK_a ~ 18) was added to **6**Fe$(CO)_2$ in CD_3CN and the averaged pK_a value of 17.1 was determined. In the contrary, due to the poor solubility of **7**Fe$(CO)_2$ in CD_3CN, [**H7**Fe$(CO)_2$]$[BPh_4]$ was prepared separately and titrated with Et_3N, yielding an averaged pK_a value of 18.3. The experiment was repeated with pyrrolidine (pK_a = 19.56), resulting in consistent pK_a values of 18.53 and 18.54 for the $[^{Pyrr}NH]^+$ in **7**.

3.2 Characterization of Hemilabile Ligand

The redox activity of **6**Fe$(CO)_2$ and **7**Fe$(CO)_2$ was probed by cyclic voltammetry, scanning two individual events near the open circuit potential (OCP) which were expected for PDI complexes. In the symmetric such as Fe(^{iPr}PDI)$(CO)_2$, one of these events was ascribed to the one-electron ligand oxidation, and the other was ascribed to the one-electron metal-based reduction resulted from metal-ligand cooperativity (Figure 3.3). Other asymmetric Fe(PDI)$(CO)_2$ complexes also revealed behaviors closely similar to Fe(^{iPr}PDI)$(CO)_2$, such as the previously reported **8**Fe$(CO)_2$ (**8** = didpa). The small deviation in the redox potentials was attributed to the uncoupled nature in the PDI backbone.

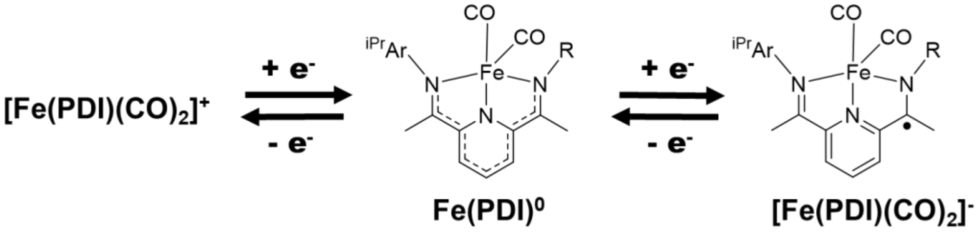

Figure 3.3 Reduction of Fe[PDI]^0. The signle electron is represented by the dot (•).

While the characteristic oxidation and reduction events were probed in **6**Fe$(CO)_2$ and **7**Fe$(CO)_2$ (SI F), unusual kinetic behavior was identified in the ligand oxidation events. In **6**Fe$(CO)_2$ and **7**Fe$(CO)_2$, distinct scan rate dependence was observed during i_p vs. (scan rate)$^{1/2}$ measurements (Figure 3.4). Normally, the ligand oxidation event is reversible when coordinating solvent such as MeCN is avoided. Unlike **8**Fe$(CO)_2$, electron transfer to the $[PDI]^{2-}$ to $[PDI]^{-}$ in **6** and **7** were rate limited; at slower scan rates, the couple was irreversible in DCM and became reversible at faster scan rates.

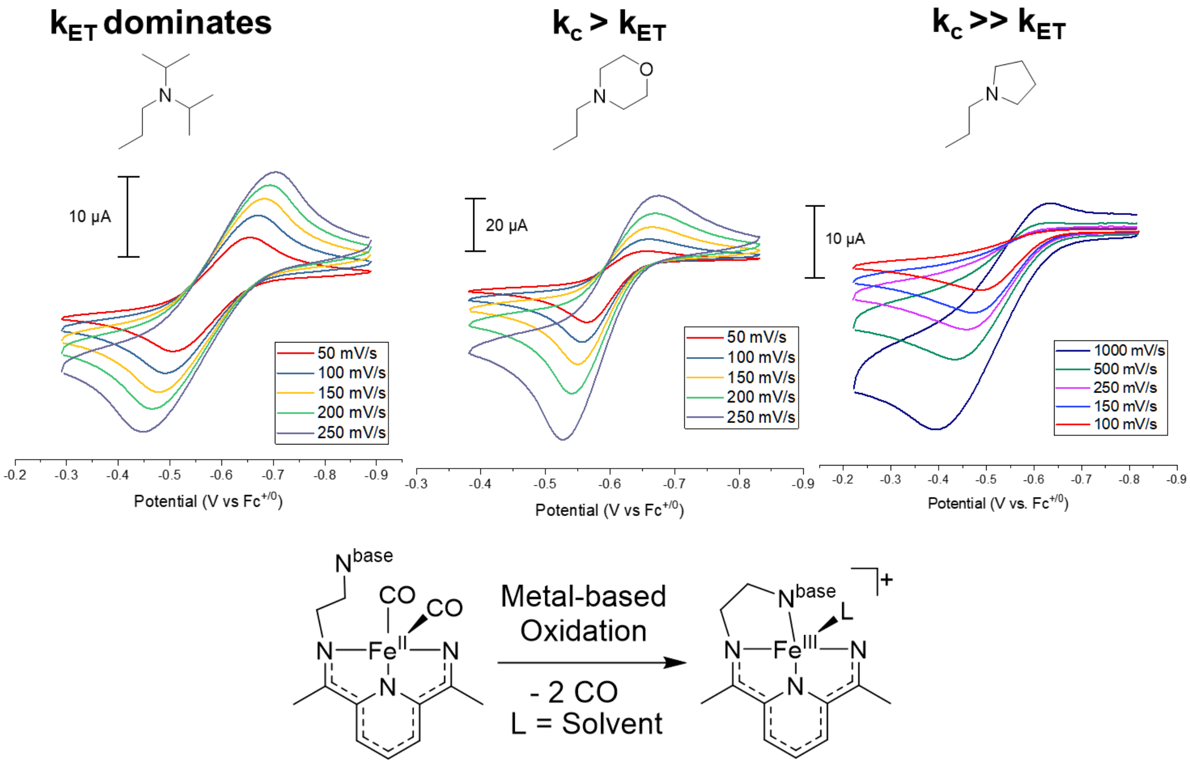

Figure 3.4 Cyclic voltammograms of **6**Fe(CO)$_2$, **7**Fe(CO), and **8**Fe(CO) in DCM (from left to right). The change from "open" to "closed" is proposed to occur when N^{base} binds to the oxidized iron center.

As shown in Figure 3.4, when **6**Fe(CO)$_2$ was scanned faster, i_{pc}/i_{pa} became closer to 1. Similarly, the reversibility in **7**Fe(CO)$_2$ was gradually restored as the scan rate was increased to 1000 mV/s, although not as pronounced as in **6**Fe(CO)$_2$. The scan rate dependence in these two experiments corresponded to the E_rC_i mechanism, where the reversible electron transfer was followed by irreversible chemical step presumed to be the coordination of pendant nitrogen to the metal center. The response to scan rates observed in **6** and **7** was indicative of their different association and dissociation equilibrium of hemilabile ligand and the competition between k_c and k_{ET}.

Additionally, a “closed” form similar to the product in Figure 3.4 can be synthesized separately by adding **7** to $Fe(OTf)_2$. While the preparation method was analogous to **7**$FeCl_2$, the product of **7**$Fe(OTf)_2$ was visibly red instead of blue. The preliminary X-ray crystal structure of **7**$Fe(OTf)_2$ revealed that the ^{pyrr}N was coordinated to the iron center, forming a six-coordinate complex with two axial OTf ions. This result was complementary to the rate-limiting effect observed in the voltammograms as the structure of **7**$Fe(OTf)_2$ elucidated the product formed during the irreversible chemical step, which was evidential to the hemilabile property when the complex is less electron-rich.

Chapter 4 – Nitrite Reduction

4.0 Proton Coupled Electron Transfer

One crucial implication of the interactions with proximal ligands in the active site of metalloenzymes is to regulate proton-coupled electron transfer (PCET) with specific rate and selectivity enhancement. Encompassing the oxidation states of nitrogen from 5+ (nitrate) to 3- (NH_3), the redox processes navigating among these nitrogen species are highly pH dependent. For example, as shown in Table 4.1, the reduction from NO_2^- to $NO^{\bullet}$ ranges from 1 V in acidic conditions to -0.46 V in basic conditions,[82] and the subsequent reduction of $NO^{\bullet}$ is governed by the acidity of the solution. Generally, a basic or acidic environment can enhance the reducing or oxidizing power, respectively, of NOx species. When a strong enough reductant is available, the reduction from $NO^{\bullet}$ to NO^- can be driven by the formation of HNO under acidic conditions. Otherwise, the formation of N_2O is much more favorable than NO^- under acidic conditions, as protonation on NO_x promotes the N-O bond cleavage.

Table 4.1 Reduction potentials of selected reactions in the nitrogen cycle.

	Condition	E˚ (V vs NHE)	E ˚ (V vs $Fc^{+/0}$)‡	Ref
$HNO_2 + H^+ + e^- \rightarrow NO^{\bullet} + H_2O$	pH 1	1.00	0.60	82
$NO_2^- + 2H^+ + e^- \rightarrow NO^{\bullet} + H_2O$	pH 7	0.37	-0.03	82
$NO_2^- + H_2O + e^- \rightarrow NO^{\bullet} + 2OH^-$	pH 14	-0.46	-0.86	82
$2HNO_2 + 4H^+ + 4e^- \rightarrow N_2O + 3H_2O$	pH 0	1.297	0.897	83
$2NO_2^- + 3H_2O + 4e^- \rightarrow N_2O + 6OH^-$	pH 14	0.15	-0.55	83
$NO^{\bullet} + H^+ + e^- \rightarrow HNO$	pH 7	-0.684	-1.084	84
$NO^{\bullet} + e^- \rightarrow NO^-$	pH 10	-0.768	-1.168	84
$2NO^{\bullet} + 2H^+ + 2e^- \rightarrow N_2O + H_2O$	pH 0	1.59	1.19	83
$2NO^{\bullet} + H_2O + 2e^- \rightarrow N_2O + 2OH^-$	pH 14	0.79	0.39	83

‡Ferrocene standard from literature ($E_{1/2}$ = 0.400 V vs NHE in MeCN) was used.[84]

The dependence on proton association is also manifested in the hydrophobic core of metalloenzymes, where protons are made accessible in proximity via the H-bonding network in the secondary coordination sphere. An analogous effect facilitating proton-couple PCET can be achieved by integrating the electron storing PDI with a hemilabile proton responsive ligand. The pendant base allows the entry of protons, and the hemilability enhance the displacement of activated substrates. According to the estimated E° values referenced to ferrocene in Table 4.1, the electron from the one-electron ligand oxidation of $Fe(PDI)(CO)_2$ ($E_{1/2}$ = ~-0.5 – 0.6 V vs Fc) can be used in the transformation of one equivalent of NO_2^- to $NO^\bullet$.

Scheme 4.1 PDI systems reported with nitrite reduction activity.

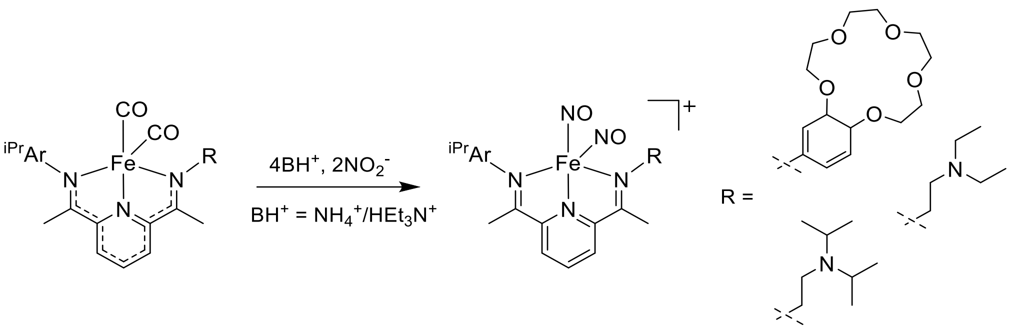

4.1 Characterization of Dinitrosyl Iron Complexes (DNICs)

The treatment of NO_2^- with the previously reported $(PDI)Fe(CO)_2$ systems has been determined to yield the corresponding dinitrosyl iron complex (DNIC) (Scheme 4.1).[49,85,86] These DNICs have been described as $\{Fe(NO)_2\}^9$ using the Enemark-Feltham (E-F) notation.[87] The superscript is the sum of the total number of Fe^0 d electrons and the pi* electrons from two $NO^\bullet$ ligands subtracted by the cationic charge of the entire unit (8 + 1 + 1 -1 = 9).

Scheme 4.2 Synthesis of DNICs.

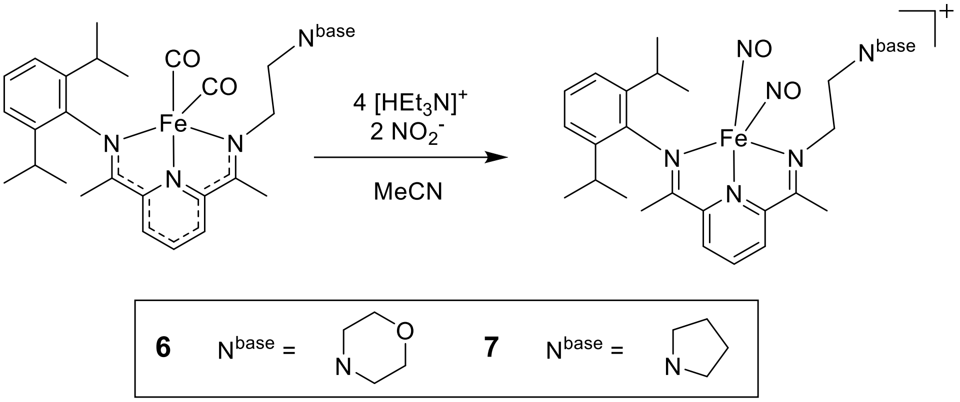

Using **6**Fe(CO)$_2$ and **7**Fe(CO)$_2$, two new DNICs were synthesized in a THF/MeOH solvent mixture with 2 equivalents of NaNO$_2$ and 4 equivalent of [NH$_4$][BPh$_4$] or [HEt$_3$N][BPh$_4$]. The products, namely [**6**Fe(NO)$_2$][BPh$_4$] and [**7**Fe(NO)$_2$][BPh$_4$] were isolated in 30% yield after a series of purification and re-crystallization. X-ray quality crystals were obtained from the spectroscopically pure products. Experimental data of [**6**Fe(NO)$_2$][BPh$_4$] and [**7**Fe(NO)$_2$][BPh$_4$], including the bond lengths, bond angles, $E_{1/2}$ values and IR stretches, are consistent with other PDI DNICs.[49,85,86] The differences between the asymmetric and symmetric νNO frequencies (ΔνNO, Table 4.2) fit in the mononuclear five-coordinate DNIC category.[88]

Table 4.2 **Values of τ_5 and ΔνNO for [6Fe(NO)$_2$][BPh$_4$] and [7Fe(NO)$_2$][BPh$_4$].**

	[**6**Fe(NO)$_2$][BPh$_4$]	[**7**Fe(NO)$_2$][BPh$_4$]
τ_5	0.32	0.24
ΔνNO (MeCN, cm^{-1})	72	74
ΔνNO (ATR, cm^{-1})	74	69
Δν^{15}NO (ATR, cm^{-1})	72	70

Additionally, the electronic states of [**6**Fe(NO)$_2$][BPh$_4$] and [**7**Fe(NO)$_2$][BPh$_4$] have been recently investigated using broken-symmetry density functional theory (BS-DFT), re-iterating the E-F assignment of {FeNO}^{9} with a PDI^0 scaffold.[89] Based on the Kohn-Sham reference, the optimized geometry suggested a S = ½ configuration with a formal assignment of [(PDI^0)Fe^{II}(NO$^•$)(NO$^-$)]$^+$, but the BS solution did not exclude the multireference character, given the configuration of [(PDI^0)Fe^{III}(NO$^-$)$_2$]$^+$ could also fit in the {FeNO}^{9} description.[89,90]

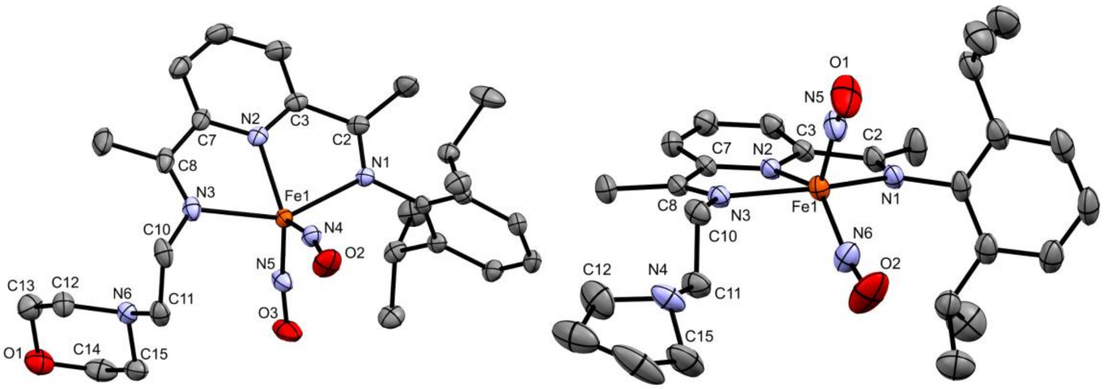

Figure 4.1 Solid state structures of [**6**Fe(NO)$_2$][BPh$_4$] and [**7**Fe(NO)$_2$][BPh$_4$]. ORTEP view at ellipsoid probability of 50%. For clarity, [BPh$_4$]$^-$ and all H atoms have been omitted. C$_{imine}$–N$_{imine}$ bond lengths: 1.280(3) and 1.290(3) Å in [**6**Fe(NO)$_2$][BPh$_4$]; 1.283(2) and 1.285(2) Å in [**7**Fe(NO)$_2$][BPh$_4$]. C$_{imine}$–C$_{ipso}$ bond lengths: 1.486(4) and 1.483(5) Å in [**6**Fe(NO)$_2$][BPh$_4$]; 1.488(3) and 1.488(3) Å in [**7**Fe(NO)$_2$][BPh$_4$]. Both exhibit FeNO in the attracto conformation.

4.2 **Kinetics of Nitrite Reduction**

The reaction in CH$_3$CN with 2 equiv. of TBANO$_2$ and 4 equiv. of [HEt$_3$N][BPh$_4$] were monitored spectroscopically. The initial rates for the decay of **6**Fe(CO)$_2$ and **7**Fe(CO)$_2$ obtained from the UV-Vis kinetics were 2.30 x 10^{-8} Ms^{-1} and 7.07 x 10^{-8} Ms^{-1}, respectively. To compliment the kinetics data, the product(s) in these reactions were determined using IR spectroscopy to observe the formation of vNO. When the reaction of **7**Fe(CO)$_2$ + 4[HEt$_3$N][BPh$_4$] + 2TBANO$_2$ was monitored by liquid IR (Figure 4.2), an intermediate was identified as a broad band at 1667 cm^{-1} appeared, prior to the formation of DNIC vNO. The poor line shape of the band at 1667 cm^{-1} was due to the precipitation in the liquid cell during the formation of the mononitrosyl intermediates. These liquid IR data also suggested that the DNIC products formed in solution (CH$_3$CN) had the same solid state structures of [**6**Fe(NO)$_2$][BPh$_4$] and [**7**Fe(NO)$_2$][BPh$_4$] (Figure S18 and S29).

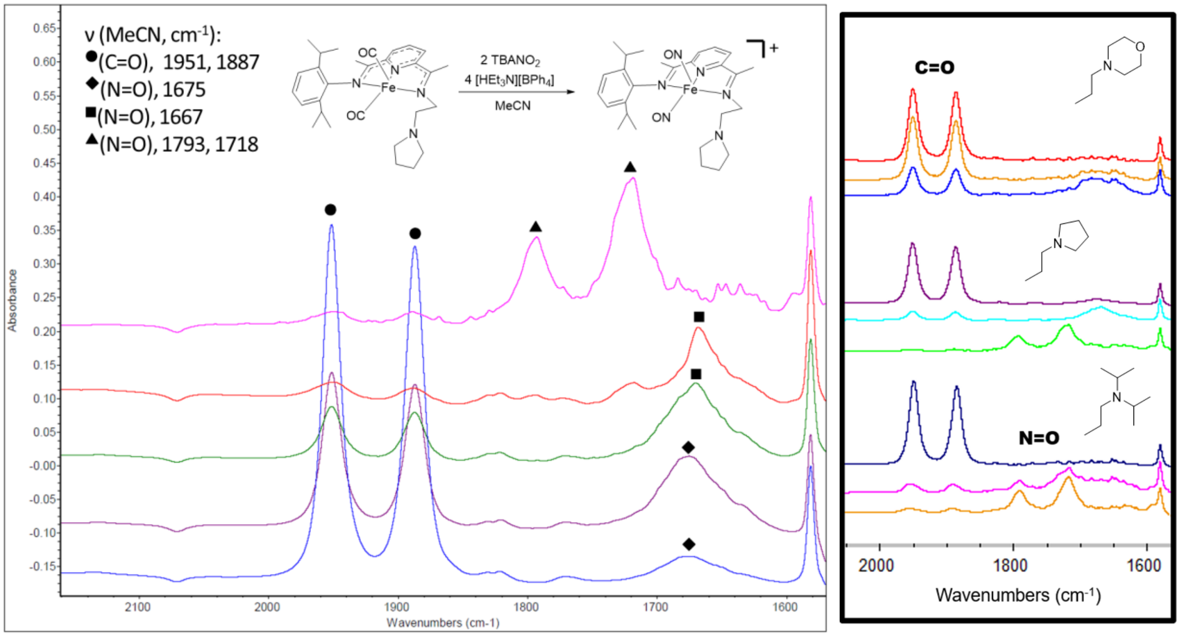

Figure 4.2 Reactions of 4[HEt$_3$N][BPh$_4$] + 2TBANO$_2$ monitored in solution IR (CH$_3$CN): (left) with **7**Fe(CO)$_2$ and (right) stack view with **6**Fe(CO)$_2$, **7**Fe(CO)$_2$ and **8**Fe(CO)$_2$.

4.3 Characterization of Mononitrosyl Iron Complexes (MNICs)

Adjusting the reaction stoichiometric ratio to 1:1:2 [**7**Fe(CO)$_\mathbf{2}$: NO$_2^-$: 2H$^+$] led to an almost exclusive formation of MNIC ([**7**FeNO]$^+$). The formation of [**7**FeNO][BPh$_4$] was presumably driven by its insolubility in both polar and non-polar solvent. The crystals of [**7**FeNO][BPh_4] were insoluble in alcohols, including MeOH, EtOH and isopropyl alcohol, as well as Et_2O and pentane. Hence [**7**FeNO]$^+$ can be easily purified by washing with these solvents. A similar result was obtained when reacting **6**Fe$(CO)_2$ with NO_2^- and $2H^+$ with the exception of [**6**FeNO][BPh_4] being soluble in most organic solvents, which is potentially an effect due to additional proton affinity of the morpholine oxygen atom. These newly identified MNIC complexes have been isolated in decent quantity, presumably due to the hemilability of the non-bulky pendant base.

Scheme 4.3 Synthesis of MNICs.

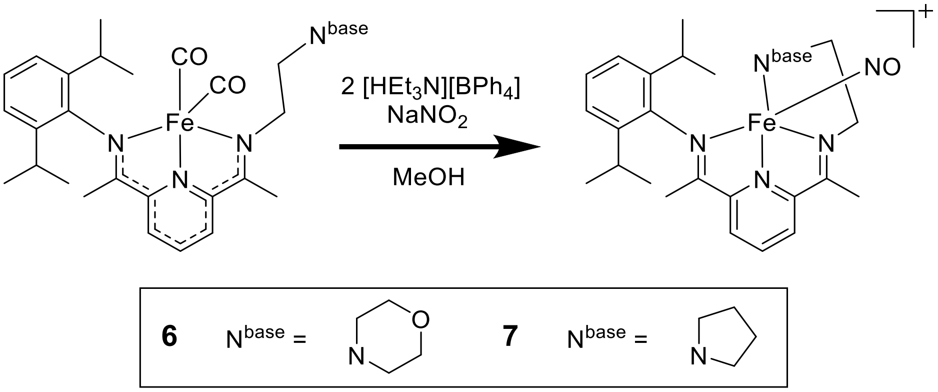

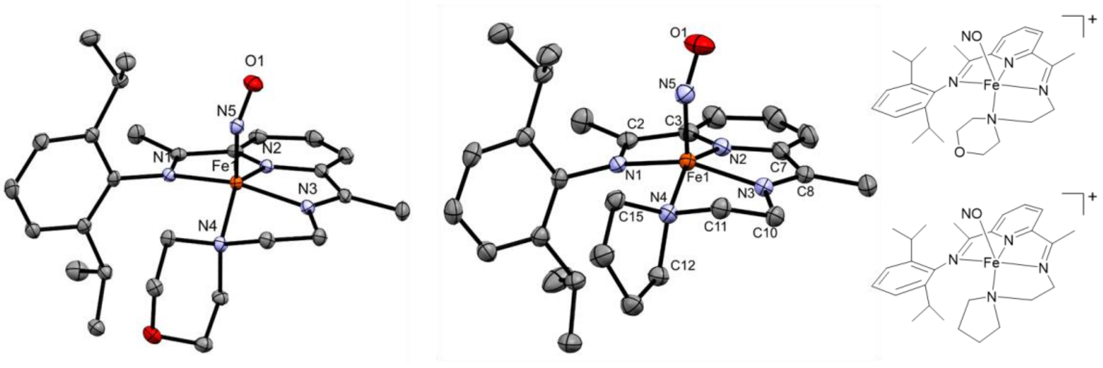

Figure 4.3 Solid state structures of (left) [**6**FeNO]$^+$ and (right) [**7**FeNO]$^+$, ORTEP rendered in view at 50% ellipsoid probability (all H-atoms and the BPh_4^- have been omitted). C_{imine}-N_{imine} bond lengths: 1.314(1) and 1.313(2) Å in [**6**FeNO]$^+$; 1.315(2)

and 1.313(2) Å in [**7**FeNO]$^+$. C_{imine}–C_{ipso} bond lengths: 1.446(2) and 1.440(2) Å in [**6**FeNO]$^+$; 1.453(2) and 1.439(2) Å in [**7**FeNO]$^+$.

Table 4.3 Selected experimental bond distances, angles of NICs.

	[**6**FeNO][BPh$_4$]	[**7**FeNO][BPh$_4$]	[**6**Fe(NO)$_2$][BPh$_4$]	[**7**Fe(NO)$_2$][BPh$_4$]
Fe—^{PDI}N1 (Å)	2.035(1)	2.031(1)	2.233(3)	2.216(2)
Fe—^{PDI}N2 (Å)	1.836(1)	1.830(2)	2.065(2)	2.080(1)
Fe—^{PDI}N3 (Å)	1.894(1)	1.894(1)	2.171(3)	2.138(2)
Fe— ^{hemi}N (Å)	2.076(1)	2.066(1)	--	--
Fe—N[O] (Å)	1.679(1)	1.677(2)	1.696(3), 1.694(2)	1.693(2), 1.696(2)
N—O (Å)	1.183(2)	1.182(2)	1.165(3), 1.168(3)	1.170(3), 1.173(3)
τ_5	0.12	0.09	0.32	0.24
∠ Fe—N—O (°)	154.4(1)	150.9(2)	162.1(2) 160.8(3)	161.9(2) 160.4(2)
∠ [O]N—Fe—N[O]	--	--	108.6(1)	108.7(1)
ν NO (MeCN, cm^{-1})	1678	1675[a]	1794, 1722	1795, 1721[b]
ν NO (ATR, cm^{-1})	1687	1667	1783, 1709	1785, 1716
ν ^{15}NO (ATR, cm^{-1})	1654	1635	1749, 1677	1752, 1682
δ (mm/s)	0.095(5)	0.042(3)	--	0.32(3)
ΔE_Q (mm/s)	0.415(9)	0.489(5)	--	0.82(9)

[a] Shifted to 1667 cm^{-1} as it precipitated as the spectrum became poorly resolved. [b] The final νNO bands upon the complete disappearance of νNO of MNIC.

Each of the solid FT-IR spectra of [**6**FeNO][BPh$_4$] and [**7**FeNO][BPh$_4$] had an intense νNO band at 1687 and 1666 cm^{-1} (ν^{15}NO = 1654 and 1635 cm^{-1}), respectively (Figure S22 and S13). This suggested that the MNIC intermediates, **6**FeNO][BPh$_4$] and [**7**FeNO][BPh$_4$], were chemically stable, and they exhibit in solution with structures virtually identical to their solid states. Both MNICs were square pyramidal (τ_5 = 0.12 for [**6**FeNO][BPh$_4$] and 0.09 for [**7**FeNO][BPh$_4$]),[80] where the hemilabile base and the PDI formed an N_4 plane. The axial NO ligand adapted an unusual angle for most iron nitrosyl complexes in both cases,[91,92] with the ∠Fe—N—O of 154.4(1)° for [**6**FeNO][BPh_4] and 150.9(2)° for [**7**FeNO][BPh_4]. Some of the important spectroscopic data of these MNICs are summarized in Table 4.3.

Unlike the ill-resolved ^1H NMR spectrum of the DNICs (Figure S19-S20 and S27-S28), the spectra of both [**7**FeNO][BPh_4] and [**6**FeNO][BPh_4] is indicative of an overall S = 0 environment in both MNICs as they show well resolved resonance that can be integrated for the total number of protons. Figure 4.4 illustrates the coupling of the pyrrolidine protons in [**7**FeNO][BPh_4] when the ^{pyrr}N coordinates to the iron center (A) in comparison to (B) and (C), where the pendant pyrrole is non-coordinating. The hemilabile effect also applies to the morpholine protons in [**6**FeNO][BPh_4] and can be monitored by ^1H NMR for future reactivity studies.

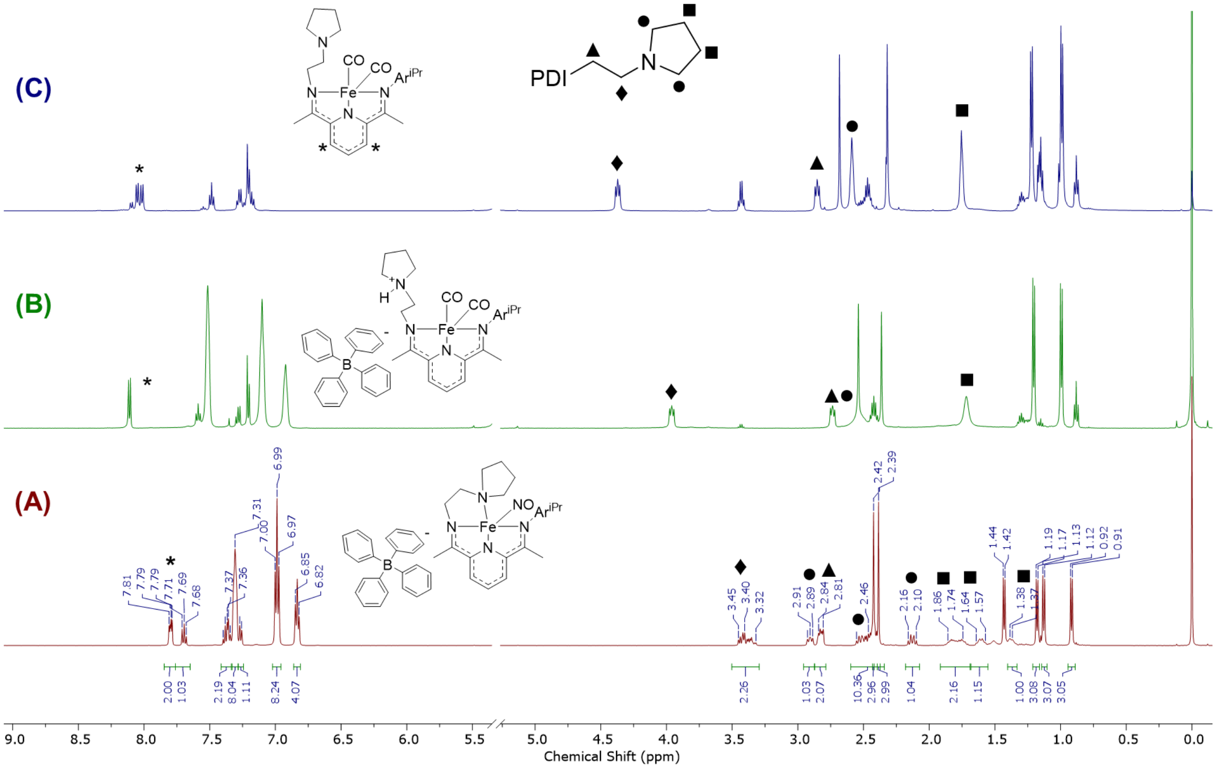

Figure 4.4 Stacked ^{1}H NMR (500 MHz) spectrum of [**7**FeNO][BPh$_4$], [**H7**Fe(CO)$_2$][BPh$_4$] and **7**Fe(CO)$_2$ (A, B and C, respectively). All recorded in CD$_2$Cl$_2$.

Mossbauer parameters, ∠Fe—N—O and νNO values were suggestive of {FeNO}^{7} with a NO$^\bullet$ ligand in **6** and **7**MNICs, contradicting to the diamagnetic behavior observed in 1H NMR, as no diamagnetic {FeNO}^{7} has been reported. In order to verify the E-F assignment for these MNICs, the electronic state of the PDI ligand were investigated. In both **6** and **7**MNICs, the C$_{\text{imine}}$-N$_{\text{imine}}$ and C$_{\text{imine}}$-C$_{\text{ipso}}$ bond lengths are similar to those observed in a reduced PDI scaffold. The presence of a reduced PDI ligand in MNICs were complimented by BS-DFT calculations, yielding the most stable solutions of BS(2,2) and BS(0,0), where the BS(*m*,*n*) notation represents the *m* electrons on the iron center antiferromagnetically coupled to the *n* electrons on the ligands. Both BS solutions indicated that the PDI is singly reduced, and the MNICs can be formally assigned as $\mathrm{Fe(II)}(\uparrow\uparrow)\mathrm{NO}^{\bullet}(\downarrow)\mathrm{PDI}^{\bullet-}(\downarrow)$ for BS(2,2) and $\mathrm{Fe(II)}(\uparrow\downarrow)\mathrm{NO}^{\bullet}(\uparrow)\mathrm{PDI}^{\bullet-}(\downarrow)$ for BS(0,0). These allows the configuration of diamagnetic $\{\mathrm{FeNO}\}^7$ as in the charge formula of $[\mathrm{FeNO}]^{2+}[\mathrm{PDI}]^{-}[\mathrm{BPh}_4]^{-}$. The superscript on the E-F notation in this case is the sum of the total number of Fe^0 d electrons and the pi* electrons from $\mathrm{NO}^{\bullet}$ subtracted by the cationic charge of the $[\mathrm{FeNO}]^{2+}$ unit (8 + 1 – 2 = 7).

4.4 Kinetic Enhancing Properties

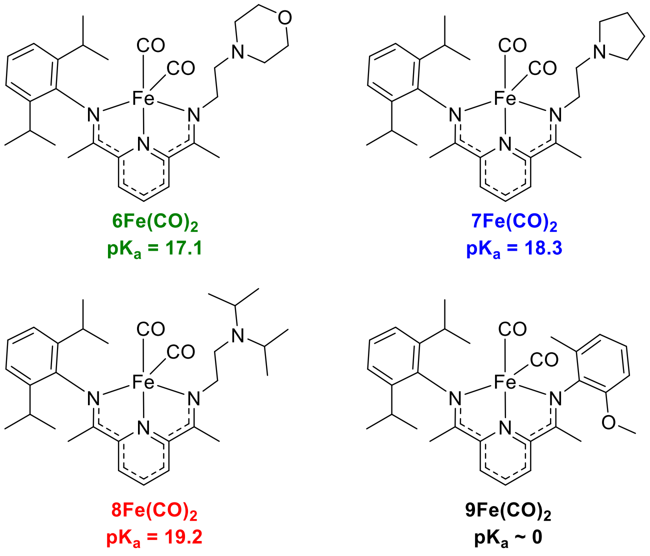

6Fe(CO)$_2$
pK_a = 17.1

7Fe(CO)$_2$
pK_a = 18.3

8Fe(CO)$_2$
pK_a = 19.2

9Fe(CO)$_2$
pK_a ~ 0

Figure 4.5 PDI complexes tested and their pK_a values in CD_3CN.

As mentioned in 4.2, the reaction in CH_3CN with 2 equiv. of $TBANO_2$ and 4 equiv. of $[HEt_3N][BPh_4]$ (pK_a = 18) monitored via UV-Vis yielded initial rates of 2.30×10^{-8} Ms^{-1} for **6**Fe(CO)$_2$ and 7.07×10^{-8} Ms^{-1} for **7**Fe(CO)$_2$. The difference in the rates is ascribed to the pK_a of the pendant base, as the more acidic pendant PDI **6** ensued the same rate as the control with no enhancement. The non-Brønsted PDI complex **9**Fe(CO)$_2$ was chosen for the control experiment, as it contains a proton-responsive ligand (H-bond forming) that does not participate in acid and base chemistry. While the acidity of **7** is virtually the same as the proton source, it pertained a much faster rate comparing to the more basic PDI, **8**.

Replacing the proton source with $[HLut][BPh_4]$ (pK_a = 14.1), a much greater rate enhancement effect relative to **9**Fe(CO)$_2$ was observed in the systems involving hemilabile PDI, namely **6** and **7**. The stronger acid increases the initial rates by 40 times for **6**Fe(CO)$_2$ and **7**Fe(CO)$_2$, while only 10 times for **8**Fe(CO)$_2$.

	[HEt$_3$N][BPh$_4$]		**[HLut][BPh$_4$]**	
Compounds	**Rate (x10^{-8} Ms^{-1})**	**Rate Relative to Control**	**Rate (x10^{-8} Ms^{-1})**	**Rate Relative to Control**
9Fe(CO)$_2$	2.11	1.00	2.52	1.19
7Fe(CO)$_2$	7.07	3.35	81.1	38.42
6Fe(CO)$_2$	2.30	1.09	84.5	40.01
8Fe(CO)$_2$	3.97	1.88	21.2	10.06

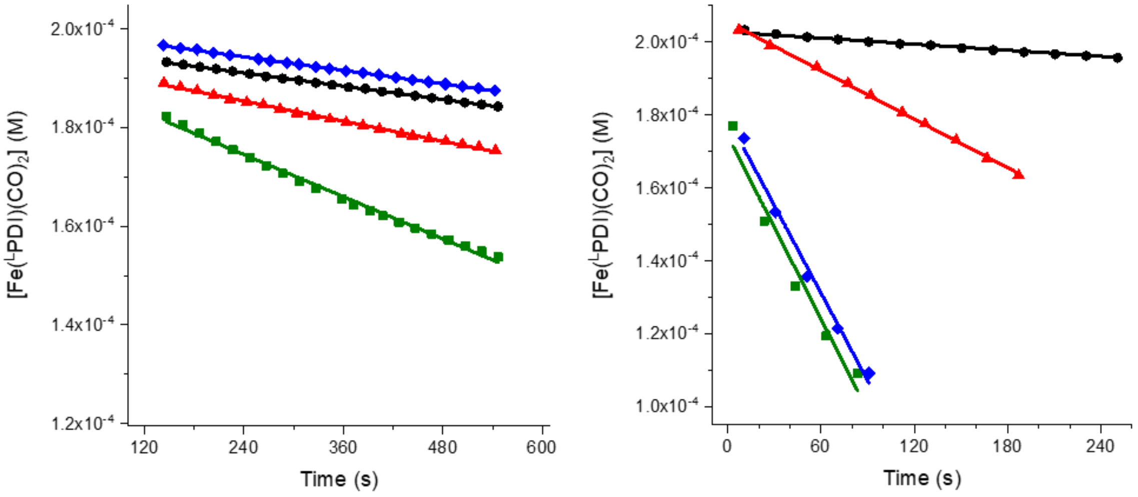

Figure 4.6 Initial rate kinetics with [HEt$_3$N]$^+$ vs [HLut]$^+$ as the acid source. Both contained [BPh$_4$]$^-$ anions. All reactions were carried out with 1:2:4 molar equivalent of [LFe(CO)$_2$: TBANO$_2$: 2H$^+$].

In summary, the kinetic experiment demonstrated the rate enhancing ability of the proton-responsive secondary coordination sphere, in agreement with the previously reported observed in pendant PDI with Brønsted acid/basicity. While the exact contribution of pK$_a$ in nitrite reduction is still underway, the kinetic data have been conclusive of the significance of hemilabile ligand.

Conclusion

Catalysis by metalloenzymes is often accompanied by the proximal access to protons near the active site. In synthetic systems, however, protonation near the metal center generally results in a prominent positive shift of redox potential, limiting electron transfer to the substrate. In order to understand the cause of this limitation, it is of our interest to investigate how the pK_a and redox potential are coupled/uncoupled in synthetic ligand scaffolds.

When functional groups are added to the system, the reduction potential of the redox active center can vary drastically, depending on the electron withdrawing/donating characteristics introduced to the ligand scaffold. In many cases where biomimetic motifs such as a Lewis acid or proton relay is incorporated, the coupling effect in proximity to the redox active center typically results in significant anodic shifts in the reduction potential. Unlike these compounds, the attenuation of reduction potential is not observed in the PDI systems with appended Lewis or Brønsted acid/bases in the secondary coordination spheres. The ligand-based reduction potential of the PDI systems is in fact conserved, regardless of the type of functional groups nearby. In previous work, the uncoupling between redox potential and secondary sphere was utilized to demonstrate the kinetic significance of encapsulated Lewis acids in the crown ether PDI system, showing that the reduction of nitrite is orders of magnitude faster with the presence of a proximal Lewis acid. The initial rate of Na^+ encapsulated $Fe(^{15c5}PDI)(CO)_2$ was 2.30 x 10^{-8} Ms^{-1}, which was about 3 times faster than without encapsulation of Na^+.[45] Under the same condition, the initial rates of 7.07 x 10^{-8} Ms^{-1} for **7**$Fe(CO)_2$ and 2.30 x 10^{-8} Ms^{-1} for **6**$Fe(CO)_2$ were comparable to the $Fe(^{15c5}PDI)(CO)_2$ studies.

The pK_a values of [**H6**Fe(CO)$_2$][BPh$_4$] and [**H7**Fe(CO)$_2$][BPh$_4$] were reiterated with other organic acids in CD_3CN, where consistent results have been obtained. The final pK_a values in acetonitrile of [**H6**Fe(CO)$_2$][BPh$_4$] and [**H7**Fe(CO)$_2$][BPh$_4$] have been determined to be 17.1 and 18.3, respectively. Using a stronger acid like [HLut]$^+$, the initial rates of nitrite reduction increased dramatically for both **7**Fe(CO)$_2$ and **6**Fe(CO)$_2$ (Figure 4.6). These results have proven the kinetic significance of protonation at the pendant bases during nitrite reduction.

Lastly, the investigation in the electrochemical properties of the Fe(CO)$_2$ and the protonated analogues had confirmed uncoupling effect between the activated secondary coordination spheres and the ligand-based redox potentials. In the **7**Fe(CO)$_2$ system, upon protonation, the ligand based redox potential was ensued in a negligible anodic shift of merely 65 mV. This finding was consistent with the previously reported PDI systems (Figure 1.5 D and E).[50] The uncoupling of the ligand-based reduction enables the utilization of PDI complexes as a versatile platform for modeling and functionalization. The ability to attain their redox allows the incorporation of cooperativity in the secondary coordination sphere, which opens avenues for designing new biomimetic models and catalysts suitable for small molecule activation.

Supporting Information

General Consideration

Most reagents for ligand synthesis, such as 1-(2-aminoethyl)pyrrolidine (≥98.0%), were purchased from TCI America and were used as received without distillation or other treatments. Tetrahydrofuran and diethyl ether were purged with N_2 for 30 mins and circulated for 6 hours in the VAC solvent purification system prior to storage. Pentane, acetonitrile, methanol and dichloromethane was dried and deoxygenated with a PureSolv solvent purification system (CuO and alumina columns). Deuterated solvents including were purchased from Cambridge Isotope Laboratories. Fresh or re-activated molecular sieves (3Å and 4Å) were added to acetonitrile and methanol for glovebox storage. All solvents, including $CDCl_3$, CD_3CN and CD_2Cl_2, were degassed before use. Air sensitive materials were handled using standard Schlenk techniques and/or stored under N_2. The following materials were synthesized according to literature procedures: $[(2,6\text{-}iPr\text{-}C_6H_3)N{=}CMe)(O{=}CMe)C_5H_3N]$,[58] $[HEt_3N][BPh_4]$,[93] $[H(2,6\text{-lutidinium})][BPh_4]$.[94]

All infrared spectra were recorded on a Thermo Scientific Nicolet iS10 FT-IR spectrometer. For general characterizations, an ATR accessory was used for solid samples. The yield determination of Fe(PDI) nitrite reduction was performed using the Smart Transmission accessory. All liquid IR samples and the solvent backgrounds were prepared under N_2 and sealed in a Teflon-capped liquid cell equipped with either NaCl or CaF_2 plates. NMR spectra were acquired using either the Unity Inova 300 MHz FT-NMR or the Bruker 500 MHz FT-NMR spectrometer. The specific operating frequencies and deuterated solvent were indicated individually. All chemical shifts were reported with respect to the internal signal of $SiMe_4$ at 0 ppm, with the exception for all the ^{19}F and ^{31}P NMR spectra, in which the chemical shifts were referenced to 1,1,1-trifluorotoluene in C_6D_6 (-63.72 ppm) and D_3PO_4 in D_2O (0 ppm), respectively. Mass spectra were collected using the Agilent GC-MS EI system equipped with a HP-5MS column (30 m x 0.25 mm x 0.25 um). UV-Vis spectra and kinetics data were obtained using the Jasco V-670 Spectrometer equipped with a Peltier controlled 6-cell linear autosampler. Cuvettes were 21-Q-10 Spectrosil® quartz from Starna Cells. All data were obtained at 298 K.

Elemental analyses were performed by ALS (formerly Columbia Analytical Services) in Tuscon, AZ. Electronic paramagnetic resonance (EPR) spectra were recorded using a Bruker EMX spectrometer equipped with an ER041XG microwave bridge, an Oxford Instrument liquid-helium quartz cryostat, and a dual mode cavity (ER4116DM). Mössbauer spectra were recorded at room temperature with a constant acceleration spectrometer (Wissel GMBH, Germany) in a horizontal transmission mode using a 50 mCi ^{57}Co source. Approximately 0.200 g of sample was crushed in a Mössbauer sample holder and a drop of Paratone-N was used to cover the sample to prevent oxidation. Data acquisition varied from 2 to 7 days to get a statistically reasonable spectrum for each sample to analyze. The velocity scale was normalized with respect to metallic iron at room temperature; hence all isomer shifts were recorded relative to metallic iron. The Mössbauer spectra were fitted by assuming Lorentzian line shapes using the NORMOS (Wissel GMBH) least-square fitting program. The isomer shift and quadrupole splitting parameters were determined from the fitted spectra.

Ligand Synthesis

[(2,6-^{i}Pr-C_6H_3)N=CMe)($C_4H_8NC_2H_4$)N=CMe)C_5H_3N] (**7**). A dry 25 mL pressure vial containing [(2,6-iPr-C_6H_3)N=CMe)(O=CMe)C_5H_3N] (1.72 g, 5.33 mmol) and excess 1-(2-aminoethyl)pyrrolidine (3.00 g, 26.3 mmol) was sealed under N_2 with a pressure lid and incubated in a silicon-based oil bath at 90°C for 36 hours. Dry MeCN was added to the resulting oil and cooled to -4°C. The precipitation was collected via filtration and washed with cold MeOH, yielding 1.56 g (70%) of pale yellow product. GC-MS (EI) [$M^{\bullet+}$] *m/z* calcd for $C_{27}H_{38}N_4$: 418.31 (100.0%), 419.31 (29.2%), 420.32 (2.7%). Found: 418.300 (100%), 419.300 (30%), 420.300 (3.5%).

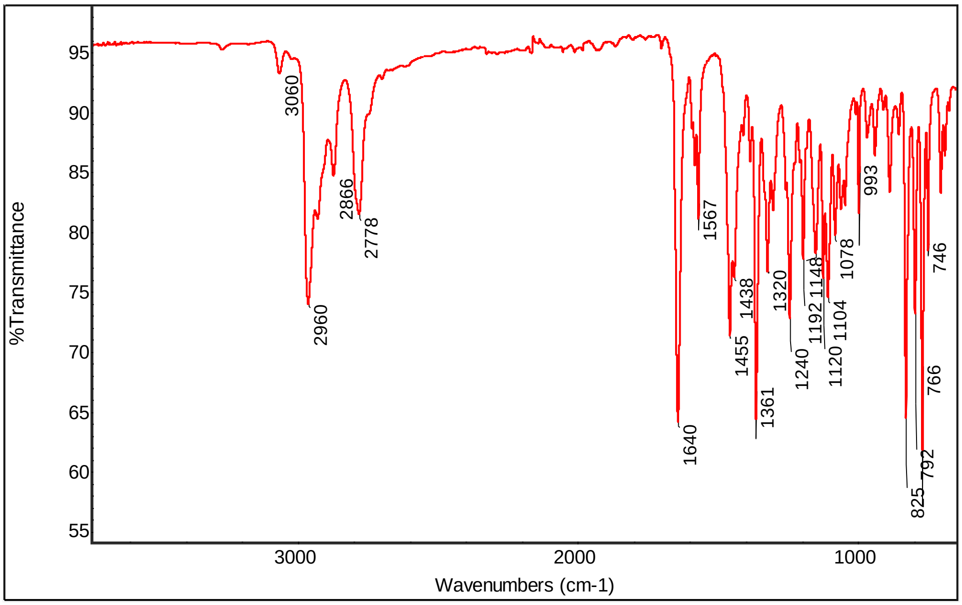

Figure S1 FT-IR (ATR): 1640 cm^{-1}(imine C=N).

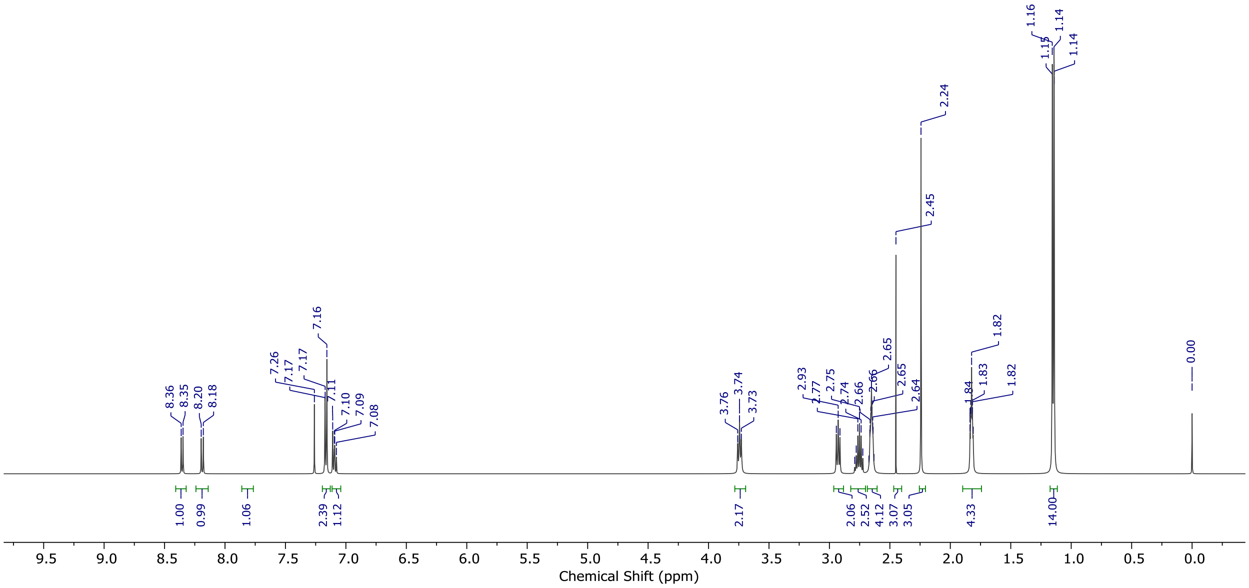

Figure S2 ^{1}H NMR (500 MHz, $CDCl_3$, δ): 8.35 (d, 1H), 8.19 (d, 1H), 7.81 (t, 1H), 7.17 – 7.08 (m, 3H), 3.74 (t, 2H), 2.94 (t, 2H), 2.79 – 2.72 (m, 2H), 2.66 – 2.64 (m, 4H), 2.45 (s, 3H), 2.24 (s, 3H), 1.84 – 1.81 (m, 4H), 1.15 (dd, 12H).

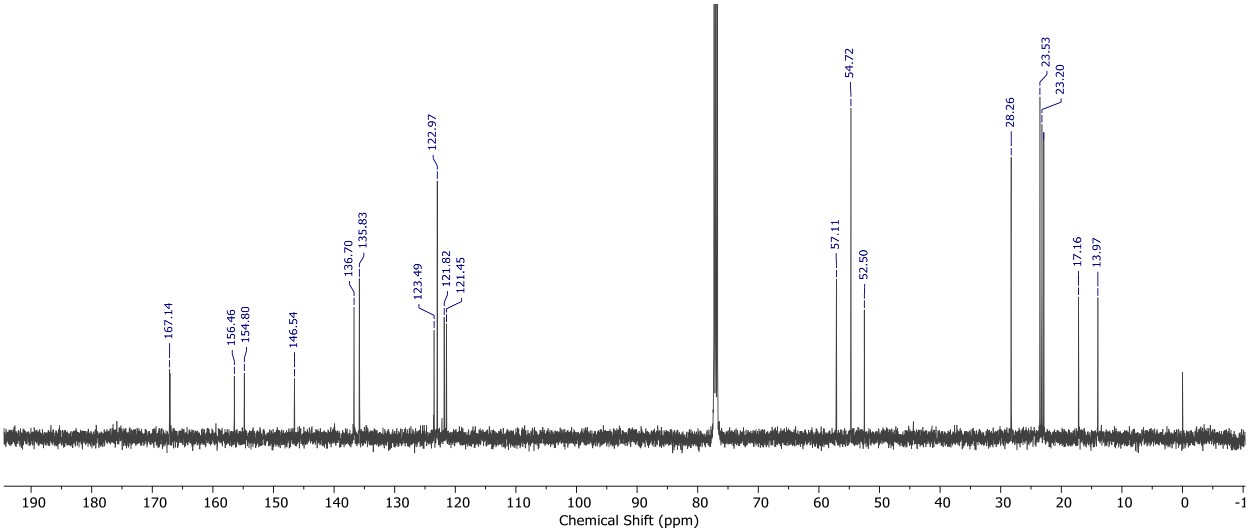

Figure S3 ^{13}C NMR (125 MHz, CDCl3, δ): 167.14, 156.46, 154.80, 146.54, 136.70, 135.83, 123.49, 122.97, 121.82, 121.45, 57.11, 54.72, 52.50, 28.26, 23.53, 23.20, 22.90, 17.16, 13.97.

Preparation of 7FeX$_2$

To a scintillation vial containing **7** (0.500 g, 1.20 mmol) and FeBr$_2$ (0.270 g, 1.25 mmol), approximately 10 mL of THF was added, resulting in an immediate color change to blue. After stirring overnight, a large amount of product precipitated in THF. A Büchner funnel was used to collect the fine precipitate upon a vacuum filtration. The collected material was washed a few times with Et$_2$O and allowed to dried, yielding 0.62 g (82%) of **7**FeBr$_2$ powder that was used subsequently without re-crystallization. FTIR (ATR): 1615, 1580 cm^{-1} (C=N). Alternatively, **7**FeCl$_2$ was prepared in the same manner with FeCl$_2$ and re-crystalized in MeOH/Et$_2$O to afforded needle-like crystals. X-ray quality crystals of **7**FeCl$_2$ were obtained by MeOH/Et$_2$O vapor diffusion.

Preparation of $7Fe(CO)_2$

To a dry Fischer-Porter tube equipped with a magnetic stir bar, **7**$FeBr_2$ (0.6195 g, 0.9767 mmol), NaHg (1.49 g, 5% Na) and 20 mL DCM was added. The tube was sealed with a pressure gauge and charged with 40 psi of CO. After vigorously stirring for 36 hours at room temperature, the reaction was then evacuated via a Schlenk line until the solvent was mostly evaporated. The crude material was treated with Et_2O, generating a dark green solution where NaHg by-products and unreacted **7**$FeBr_2$ remained insoluble. The Et_2O solution was cautiously filtered through Celite and left to evaporate overnight to afford diamond-shaped crystals of **7**$Fe(CO)_2$ (0.2937 g, 57 %). Sample was sent for elemental analysis (calculated for $C_{29}H_{38}FeN_4O_2$: C, 65.66; H, 7.22; Fe, 10.53; N, 10.56; O, 6.03).

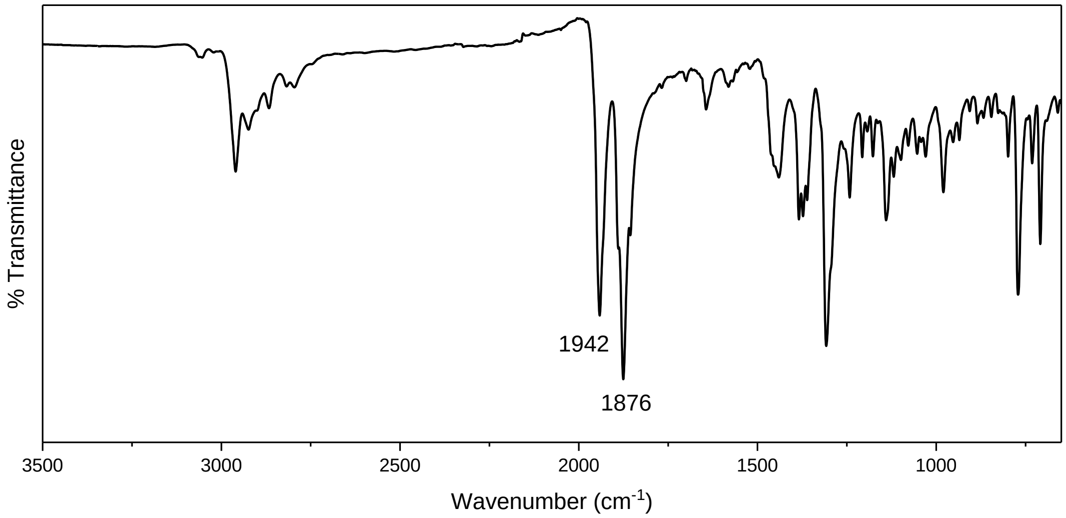

Figure S4 FT-IR (ATR): 1942, 1876 cm^{-1} (asymmetric and symmetric C=O).

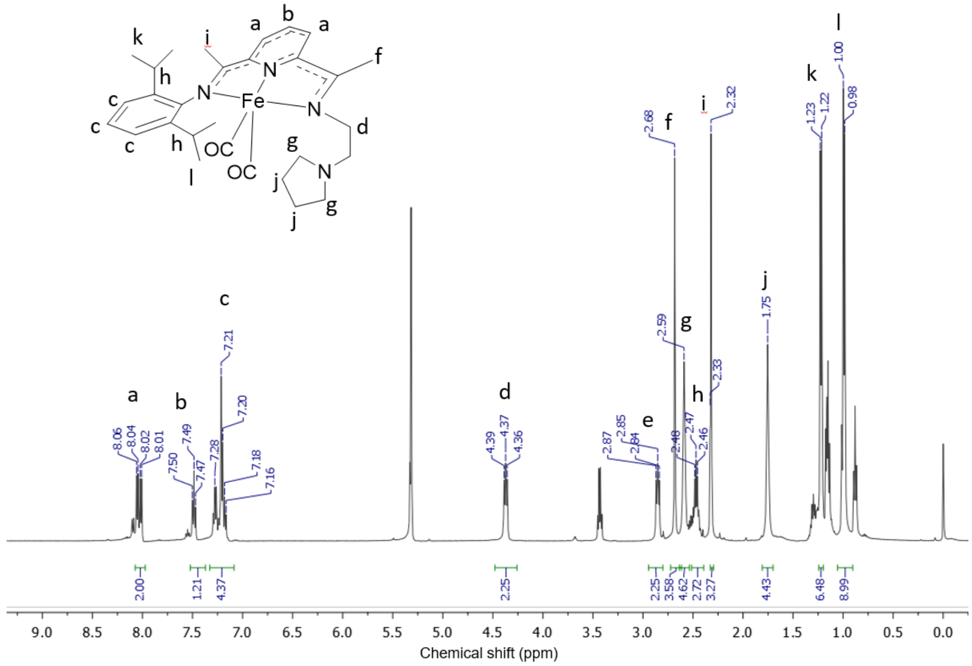

Figure S5 ^{1}H NMR (500 MHz, CD_2Cl_2, δ): 8.05 (d, 1H), 8.01 (d, 1H), 7.49 (t, 1H), 7.29 – 7.20 (m, 3H), 4.37 (m, 2H), 2.85 (m, 2H), 2.68 (s, 3H), 2.59 (br, 4H), 2.47 (m, 2H), 2.32 (s, 3H), 1.75 (br, 4H), 1.22 (d, 6H), 0.99 (d, 6H).

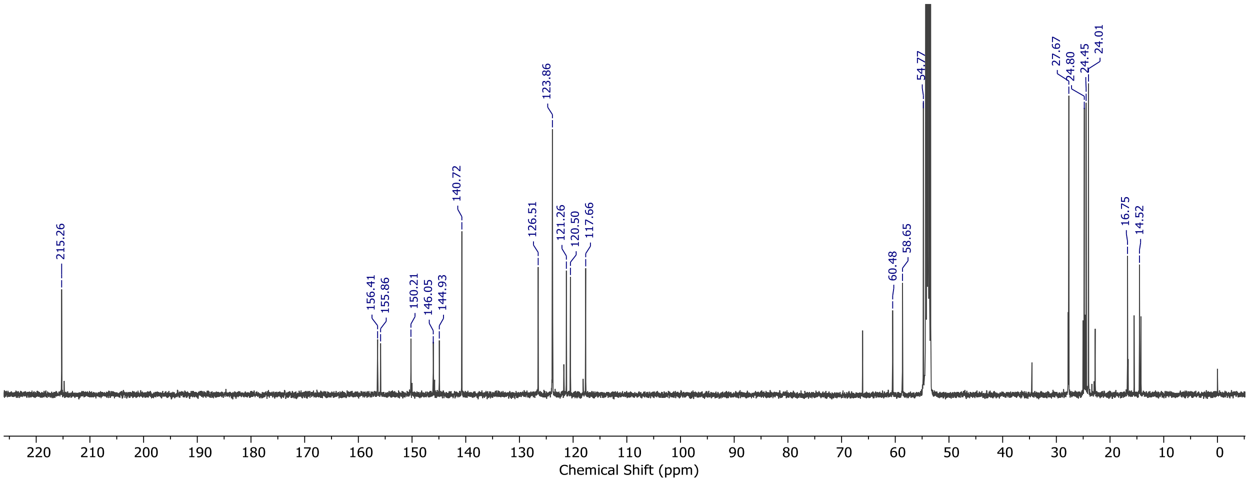

Figure S6 ^{13}C NMR (125 MHz, CD_2Cl_2, δ): 215.26 (C=O), 156.41 ($C_1=N_1$), 155.86 ($C_2=N_2$), 150.21, 146.05, 144.93, 140.72, 126.51, 123.85, 121.26, 120.50, 117.66, 60.48, 58.65, 54.77, 27.67, 24.80, 24.45, 24.01, 16.75, 14.52.

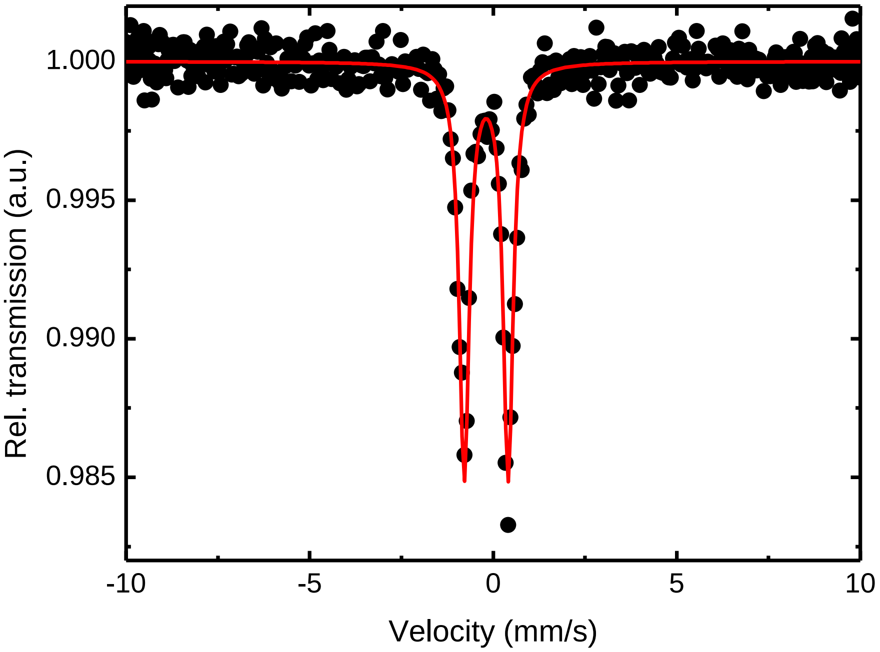

Figure S7 Zero-field Mössbauer spectrum. Isomershift, δ = -0.089(3) mm/s; quadrupole splitting, ΔE_Q = 1.197(3) mm/s; line width, Γ = 0.326(7) mm/s.

Preparation of [H7Fe(CO)$_2$][BPh$_4$]

A mixture containing **7**Fe(CO)$_2$ (0.1250 g, 0.2356 mmol) and 2 equiv. [NH$_4$][BPh$_4$] (0.1589 g, 0.4711 mmol) in 3:1 THF:MeOH was stirred overnight. The solvent was removed *in vacuo*. The resulting material was re-dissolved in DCM and filtered through Celite. The filtered solution was layered with Et$_2$O to afford crystals of [**H7**Fe(CO)$_2$][BPh$_4$] (0.1602 g, 80%).

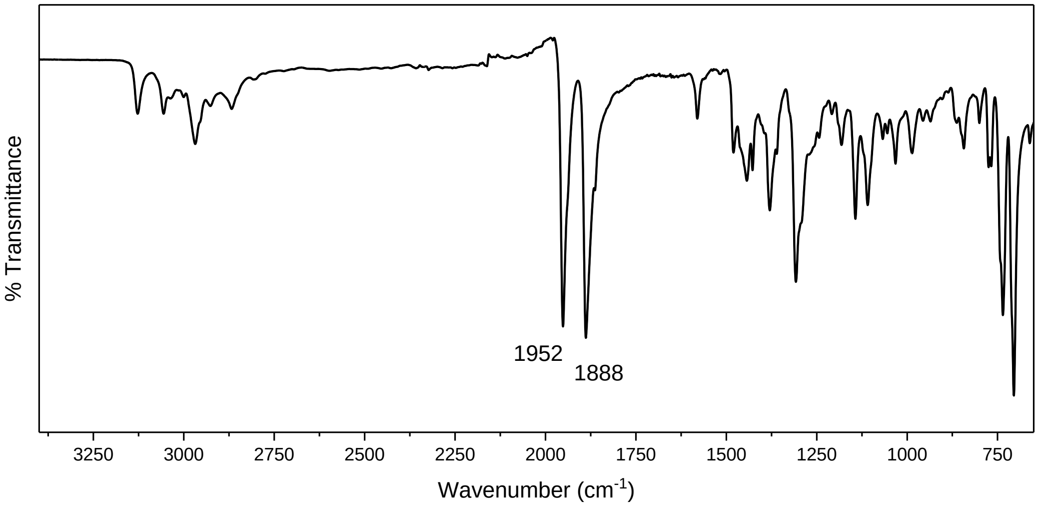

Figure S8 FT-IR (ATR): 3126 cm^{-1} (N-H); 1952, 1888 cm^{-1} (C=O); 733, 704 cm^{-1} ([$^-$BPh$_4$]).

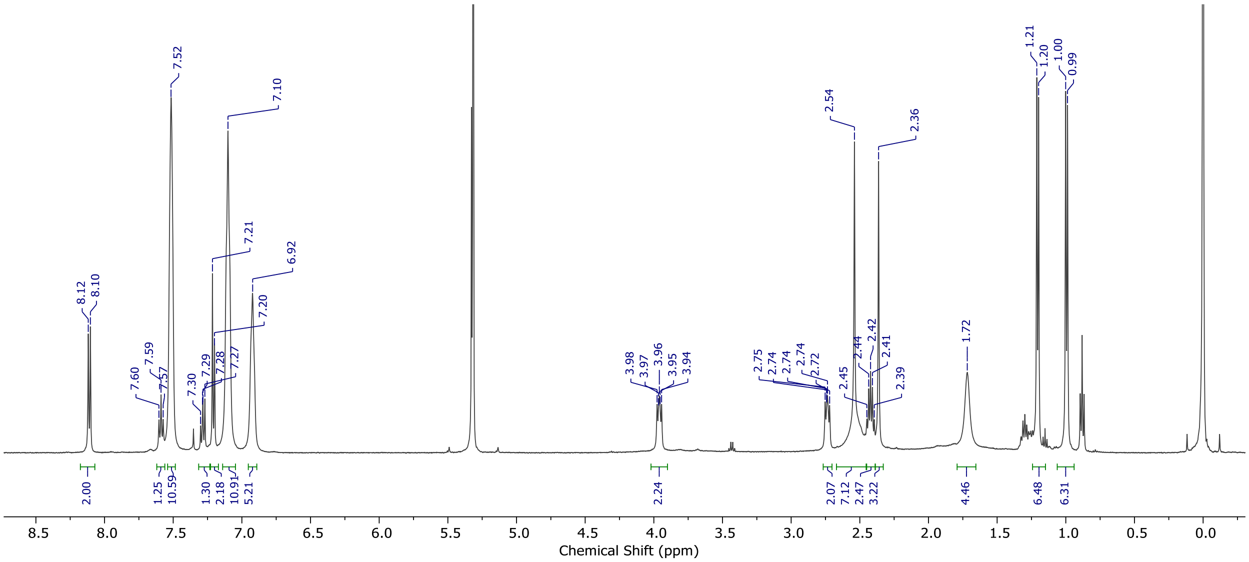

Figure S9 ^{1}H NMR (500 MHz, CD_2Cl_2, δ): 8.11 (d, 2H), 7.59 (t, 1H), 7.52 (br, 8H), 7.30 – 7.20 (m, 3H), 7.10 (br, 8H), 6.92 (br, 4H), 3.96 (m, 2H), 2.74 (m, 2H), 2.54 (s, 3H), 2.53 (br, 4H), 2.42 (m, 2H), 2.36 (s, 3H), 1.72 (br, 4H), 1.21 (d, 6H), 0.99 (d, 6H).

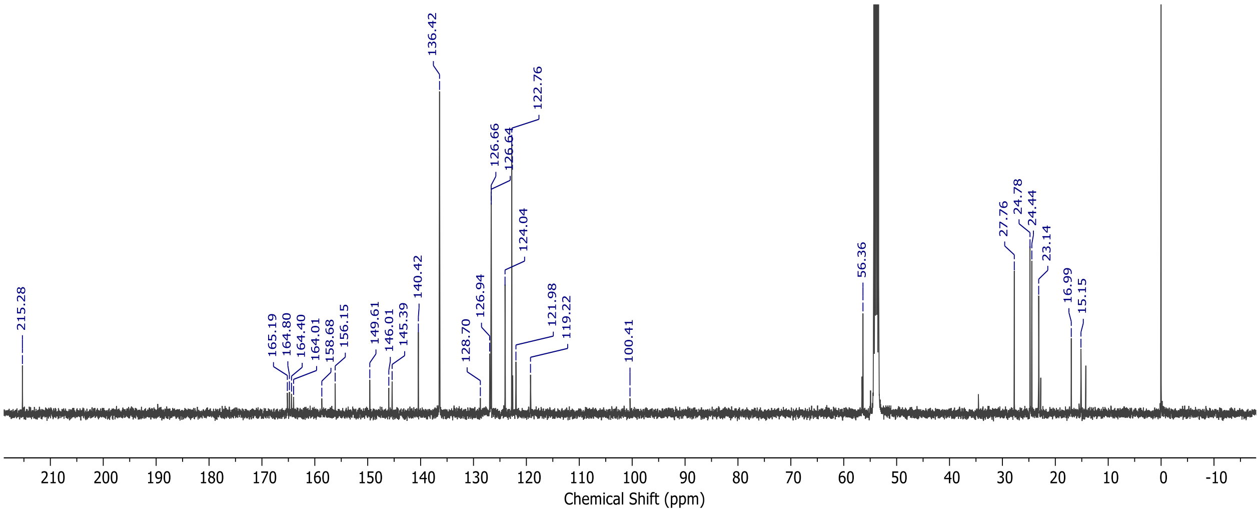

Figure S10 ^{13}C NMR (125 MHz, CD_2Cl_2, δ): 215.28 (C=O), 165.19, 164.80, 164.40, 164.01, 158.68 ($C_1=N_1$), 156.15($C_2=N_2$), 149.61, 146.01, 145.39, 140.42, 136.42, 128.70, 126.94, 126.64, 124.04, 122.76, 121.98, 119.22, 56.36, 27.76, 24.78, 24.44, 23.14, 16.99, 15.15.

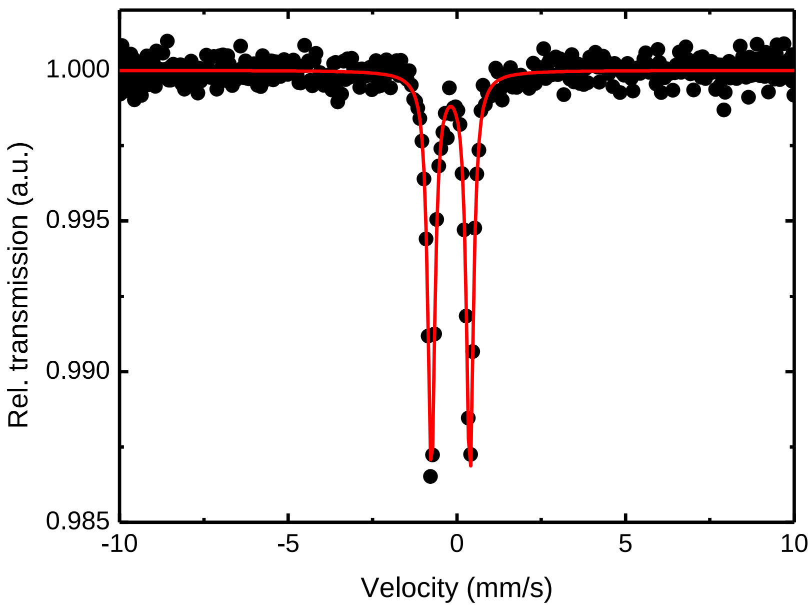

Figure S11 Zero-field Mössbauer Spectrum. Isomershift, δ = -0.084(2) mm/s; quadrupole splitting, ΔE_Q = 1.142(4) mm/s; line width, Γ = 0.246(5) mm/s.

Determination of pK_a in CD_3CN. The pK_a of [**H7**Fe(CO)$_2$][BPh_4] was measured by previously described procedures using Et_3N and pyrrolidine.[50] In acetonitrile, the pK_a of $[HEt_3N]^+$ is 18.82, and [Hpyrrolidinium]$^+$ is 19.56, according to literature.[95]

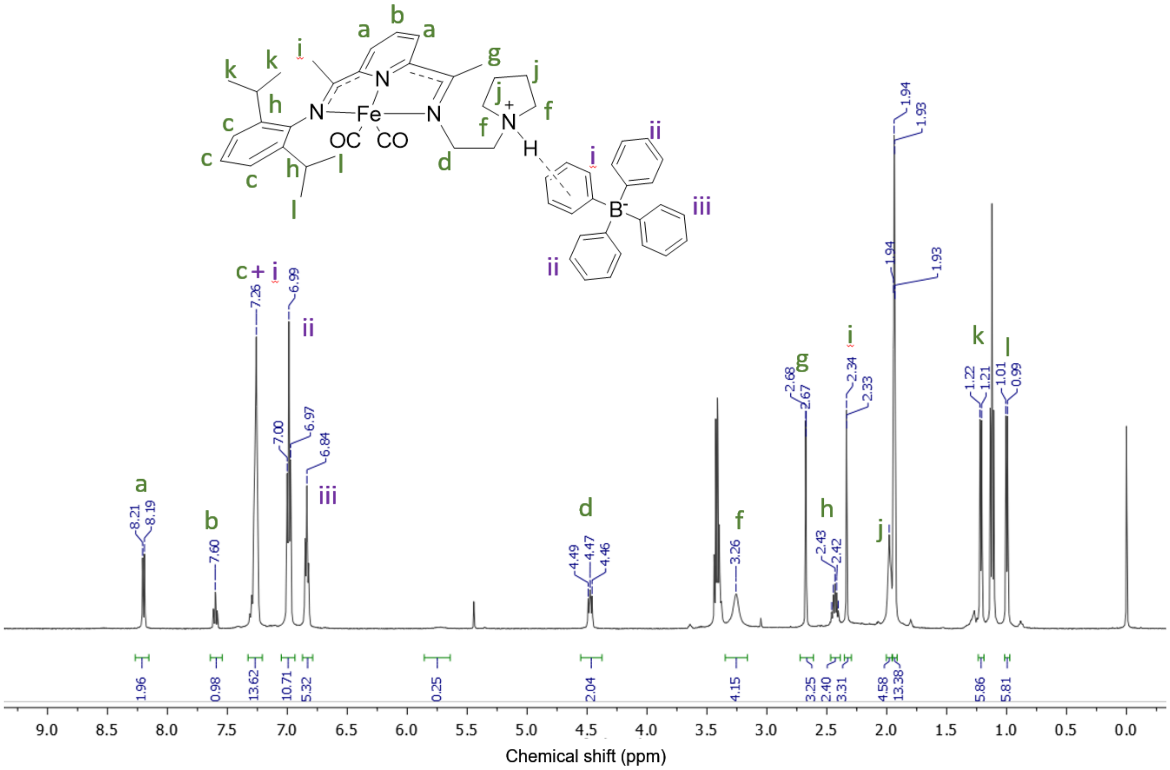

Figure S12 ^{1}H NMR in CD_3CN (500 MHz).

Nitrosyl Iron Complexes

Preparation of [7FeNO][BPh$_4$].

To a suspension of **7**Fe(CO)$_2$ (0.1575 g, 0.2970 mmol) in THF/MeOH (approximately 1:4 by volume), a MeOH solution of NaNO$_2$ (2.46 mL, 0.2970 mmol) was added. The mixture was allowed to equilibrate for about 5 minutes. While stirring, [HEt$_3$N][BPh$_4$] (0.50 g, 1.2 mmol) was added to the reaction mixture, which shortly led to the disappearance of the dark green color and eventually the formation of a blue precipitate. The solvent was then decanted into a Celite filter to isolate the precipitate, followed by treating the dried Celite mixture with DCM to re-dissolve the blue product. After filtering through a fresh Celite plug, the blue DCM solution was layered with an equal volume of Et$_2$O and left undisturbed for 3 days to afford blue crystals of [**7**FeNO][BPh$_4$] that were suitable for X-ray diffraction (0.1728 g, 71%); Anal calcd for $C_{51}H_{58}BFeN_5O$: C, 74.37; H, 7.10; B, 1.31; Fe, 6.78; N, 8.50; O, 1.94; Found: C, 73.92; H, 6.96; N, 8.40. Crystals of [**7**Fe^{15}NO][BPh$_4$] were prepared similarly using Na^{15}NO$_2$.

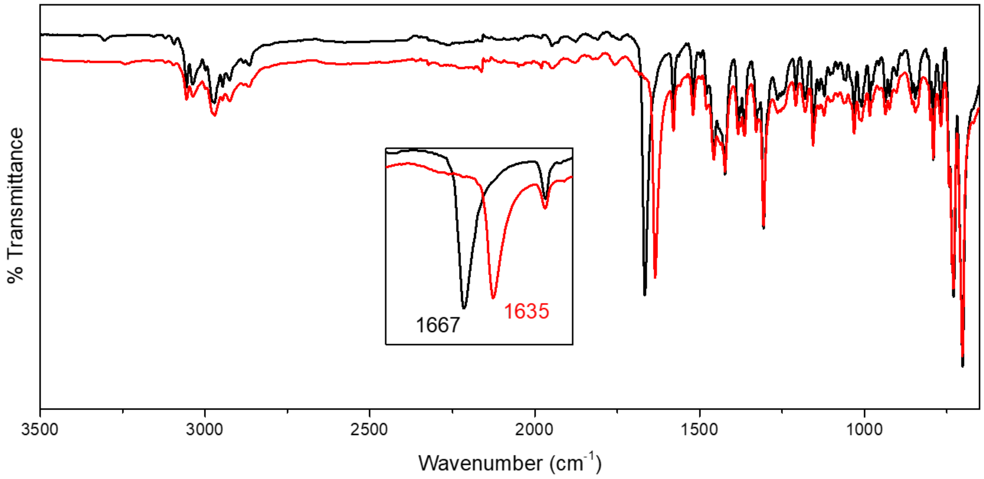

Figure S13 FT-IR (ATR, crystals) of [**7**FeNO][BPh$_4$] (black) vs. [**7**Fe^{15}NO][BPh$_4$] (red): 1667 cm^{-1} (^{14}N=O); 729, 702 cm^{-1} ([$^{-}$BPh$_4$]). ν(^{15}NO) = 1635 cm^{-1}; Δν(^{14}NO-^{15}NO) = 32 cm^{-1}.

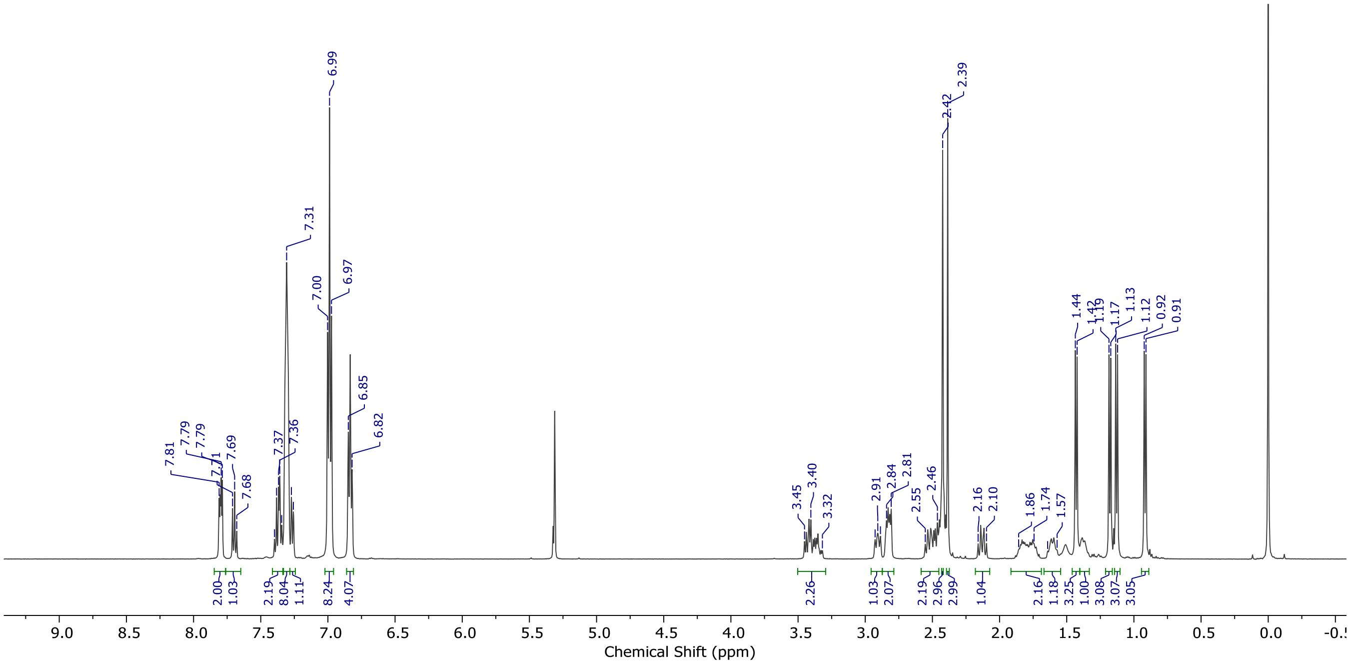

Figure S14 ^{1}H NMR (500 MHz, CD_2Cl_2, δ): 7.80 (d, 1H), 7.79 (d, 1H), 7.69 (t, 1H), 7.40 – 7.26 (m, 3H), 7.31 (br, 8H), 6.99 (t, 8H), 6.83 (t, 4H), 3.45 – 3.32 (m, 2H), 2.91 (dd, 1H), 2.84 – 2.81 (m, 2H), 2.55 – 2.46 (m, 2H), 2.42 (s, 3H), 2.39 (s, 3H), 2.13 (dd, 1H), 1.86 – 1.71 (m, 2H), 1.60 (br, 1H), 1.43 (d, 3H), 1.38 (br, 1H), 1.18 (d, 3H), 1.12 (d, 3H), 0.91 (d, 3H).

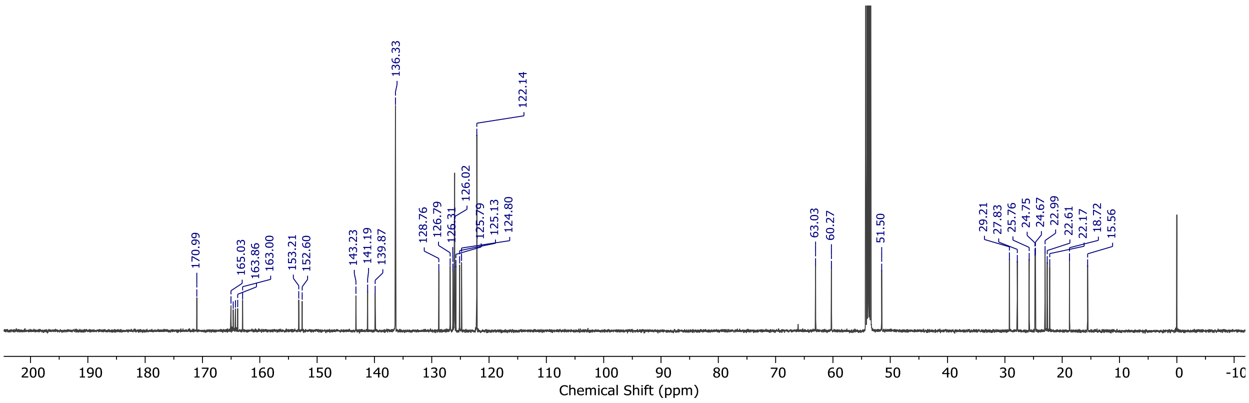

Figure S15 ^{13}C NMR (125 MHz, CD_2Cl_2, δ): 170.99 (C_1=N_1), 165.03, 164.64, 164.25, 163.86, 163.00 (C_2=N_2), 153.21, 152.60, 143.23, 141.19, 139.87, 136.33, 128.76, 126.79, 126.31, 126.02, 125.79, 125.13, 124.80, 122.14, 63.03, 60.27, 51.50, 29.21, 27.83, 25.76, 24.75, 24.67, 22.99, 22.61, 22.17, 18.72, 15.56.

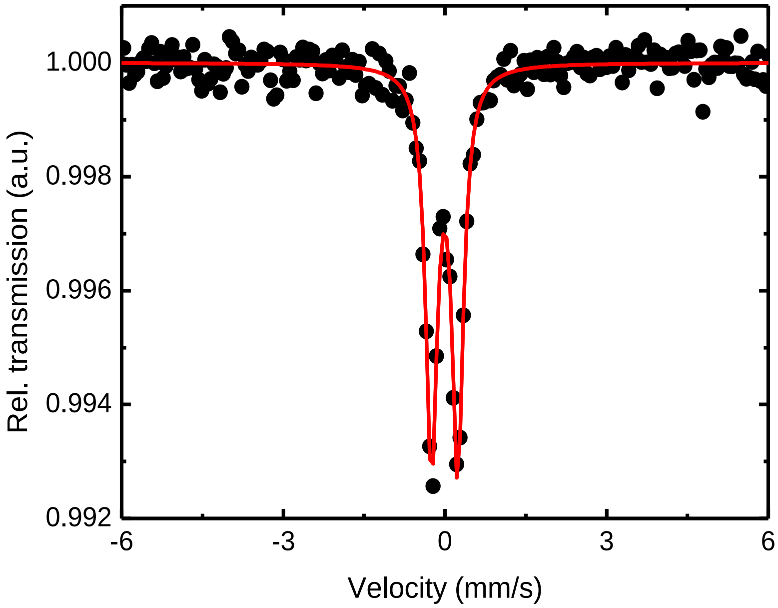

Figure S16 Zero-field Mössbauer Spectrum of [**7**FeNO][BPh$_4$]. Isomershift, δ = 0.094(3) mm/s; quadrupole splitting, ΔE_Q = 0.489(5) mm/s; line width, Γ = 0.254(7) mm/s.

Preparation of [7Fe(NO)$_2$][BPh$_4$].

To a stirring solution of **7**Fe(CO)$_2$ (0.172 g, 0.325 mmol) in THF, NaNO$_2$ (0.0454 g, 0.65 mmol) pre-dissolved in minimal MeOH was added. The mixture was left to equilibrate for about 5 minutes before adding [HEt$_3$N][BPh$_4$] (0.55 g, 1.3 mmol). A slow color change from green to brown was observed within a few hours. The reaction mixture was evacuated via a Schlenk line until all the vapor and solvents were removed. The dried-out material was then saturated with 1 – 2 mL of CHCl$_3$ (with stabilizer), causing a layer of [$^-$BPh$_4$] salts to accumulate on the solution surface, which could be removed by gravity through a Celite plug. Vapor diffusion of Et$_2$O into the brown CHCl$_3$ solution resulted in crystalline needles of [**7**Fe(NO)$_2$][BPh$_4$] (0.204 g, 76%).

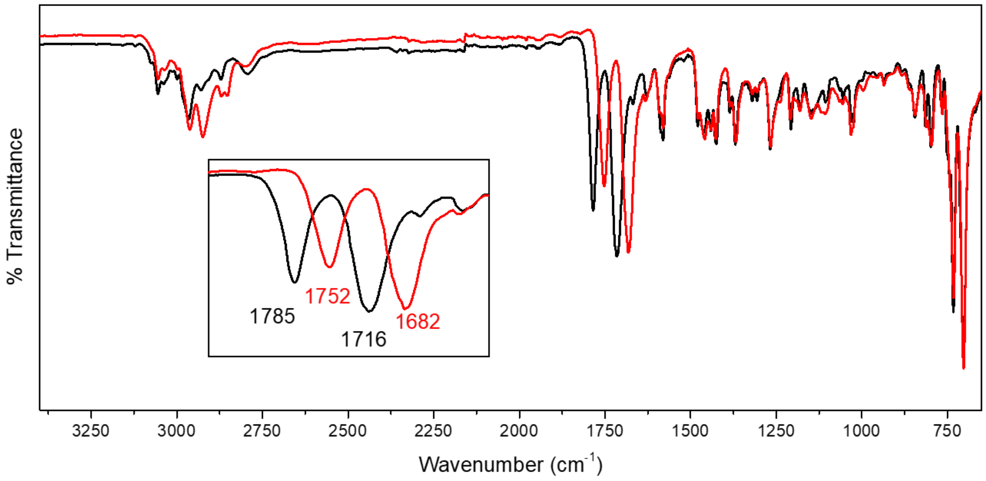

Figure S17 FT-IR (ATR) of [**7**Fe(NO)$_2$][BPh$_4$] (black) overlaid with [**7**Fe(^{15}NO)$_2$][BPh$_4$] (red): 1785, 1716 cm^{-1} (^{14}N=O); 732, 702 cm^{-1} ([$^-$BPh$_4$]). ν(^{15}NO) = 1752, 1682 cm^{-1}; Δν(^{14}NO-^{15}NO) = 32 cm^{-1}.

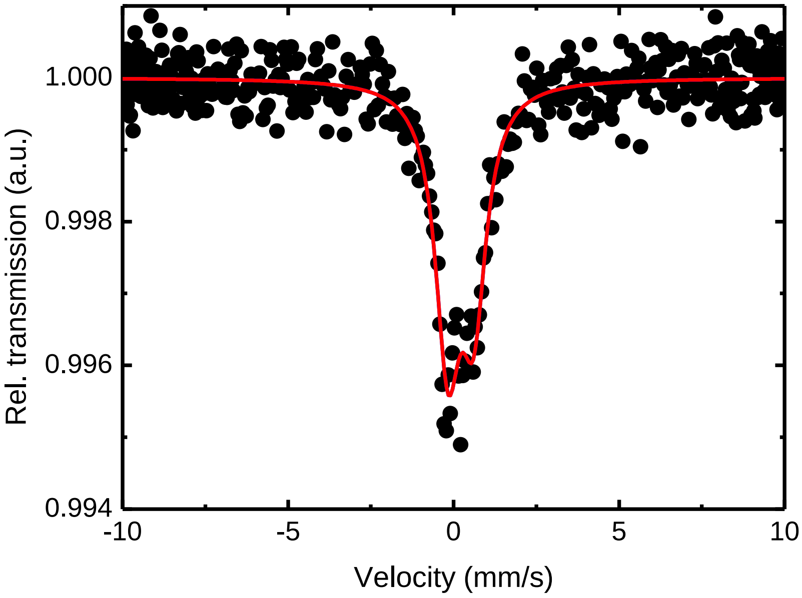

Figure S18 Zero-field Mössbauer Spectrum of [**7**Fe(NO)$_2$][BPh$_4$]. Isomershift, δ = 0.32(3) mm/s; quadrupole splitting, ΔE_Q = 0.82(9) mm/s; line width, Γ = 0.92(5) mm/s.

MNIC to DNIC. To a suspension of [**7**FeNO][BPh$_4$] (0.2031 g, 0.38 mmol) in THF, a MeOH solution containing an excess of NaNO$_2$ (0.0528 g, 0.77 mmol) was added. A color change to reddish brown was observed within a few hours of stirring. The solvent was removed via the Schlenk line. The resulting material was triturated with MeOH, followed by filtration via Celite to separate into a reddish brown solid and a brown MeOH filtrate. The solid was re-dissolved in THF and filtered again through Celite. Dark red crystals were obtained by re-crystallization in a THF solution layered with Et$_2$O (1:3 by volume THF/Et$_2$O). This method yielded 0.05 g of the said crystals (15%). More products could be obtained by combining the decanted solution. As revealed by X-ray diffraction, the dark red crystals had a structure identical to [**7**Fe(NO)$_2$][BPh$_4$] generated from **7**Fe(CO)$_2$ as described above. However, other spectroscopic data showed questionable results.

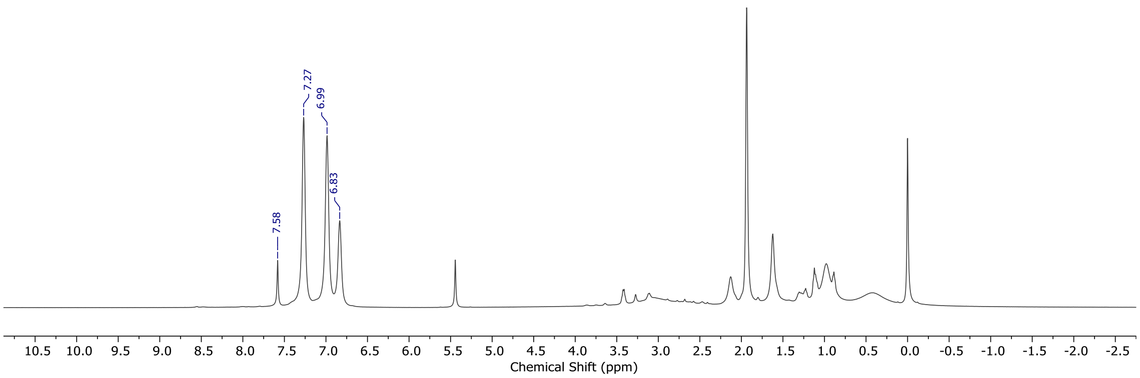

Figure S19 ^{1}H NMR (500 MHz) spectrum of [**7**Fe(NO)$_2$][BPh$_4$] in CD$_3$CN.

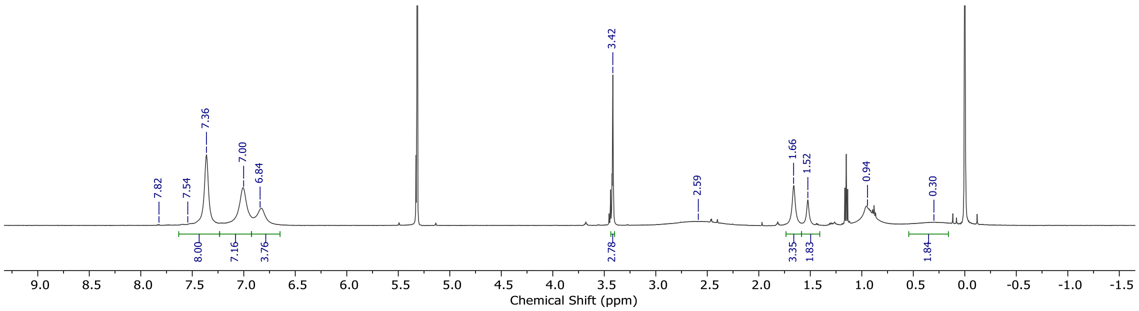

Figure S20 ^{1}H NMR (500 MHz) spectrum of [**7**Fe(NO)$_2$][BPh$_4$] in CD$_2$Cl$_2$.

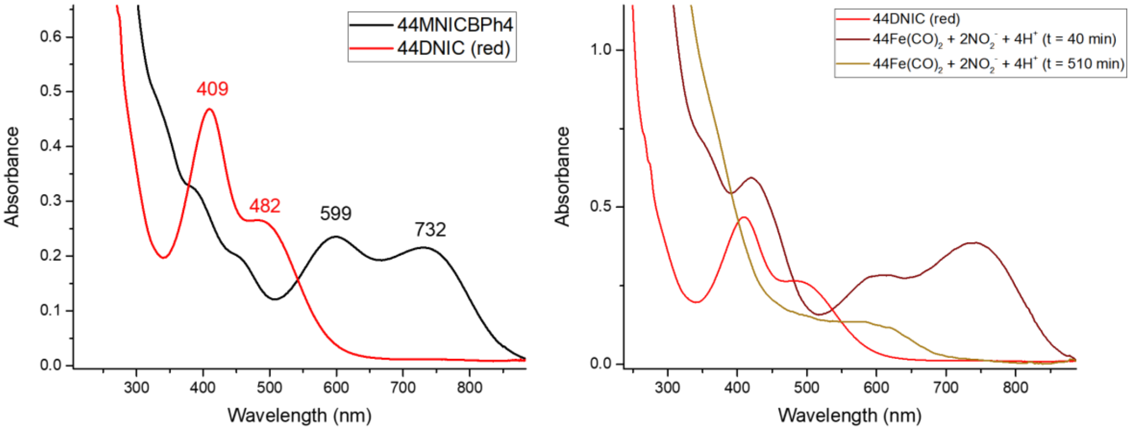

Figure S21 UV-Vis absorption. The bright red color of [**7**Fe(NO)$_2$][BPh$_4$] was attributed to the absorbance bands at 409 and 482 mn, which were not seen in [**7**Fe(NO)$_2$][BPh$_4$].prepared directly from Fe(CO)$_2$. The difference in electronic spectra may be evidential to a high spin DNIC intermediate.

Preparation of [6FeNO][BPh$_4$]

The procedure described for [**7**FeNO][BPh$_4$] was used with the following materials: **6**Fe(CO)$_2$ (0.1425 g, 0.26 mmol), NaNO$_2$ (2.16 mL, 0.26 mmol). and [NH$_4$][BPh$_4$] (0.3518 g, 1.04 mmol). The work up in DCM/Et$_2$O resulted in the co-crystallization of MNIC, DNIC and some unidentified purple solid. The purple solid was presumably [**H6**FeBr$_2$]$^+$, which could be removed by washing with MeOH until the MeOH became colorless. The remaining mixture was re-dissolved in CHCl$_3$, upon which the DNIC ([**6**Fe(NO)$_2$][BPh$_4$]) could be removed in the brown filtrate through a Celite plug. The remaining blue green solid of [**6**FeNO][BPh$_4$] was collected and re-crystallized (0.0759 g, 35%). Crystals suitable for X-ray diffraction was grown by THF/Et$_2$O vapor diffusion. Anal calcd for $C_{51}H_{58}BFeN_5O_2$: C, 72.95; H, 6.96; B, 1.29; Fe, 6.65; N, 8.34; O, 3.81; Found: C, 72.95; H, 6.93; N, 8.24.

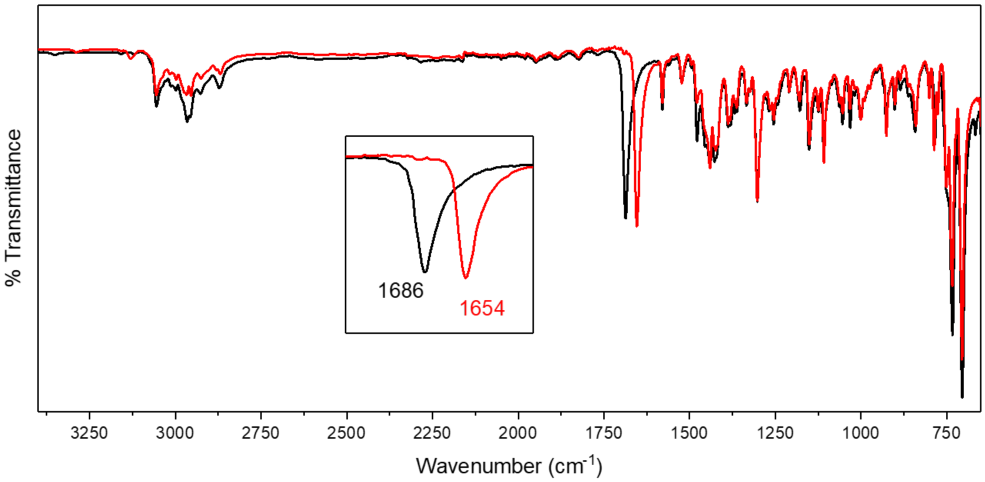

Figure S22 FT-IR (ATR) of [**6**FeNO][BPh$_4$] (black): 1686 (^{14}N=O); 734, 705 cm^{-1} ($^{-}$BPh$_4$). [**6**Fe^{15}NO][BPh$_4$] (red): ν(^{15}NO) = 1654 cm^{-1}. Δν(^{14}NO-^{15}NO) = 32 cm^{-1}.

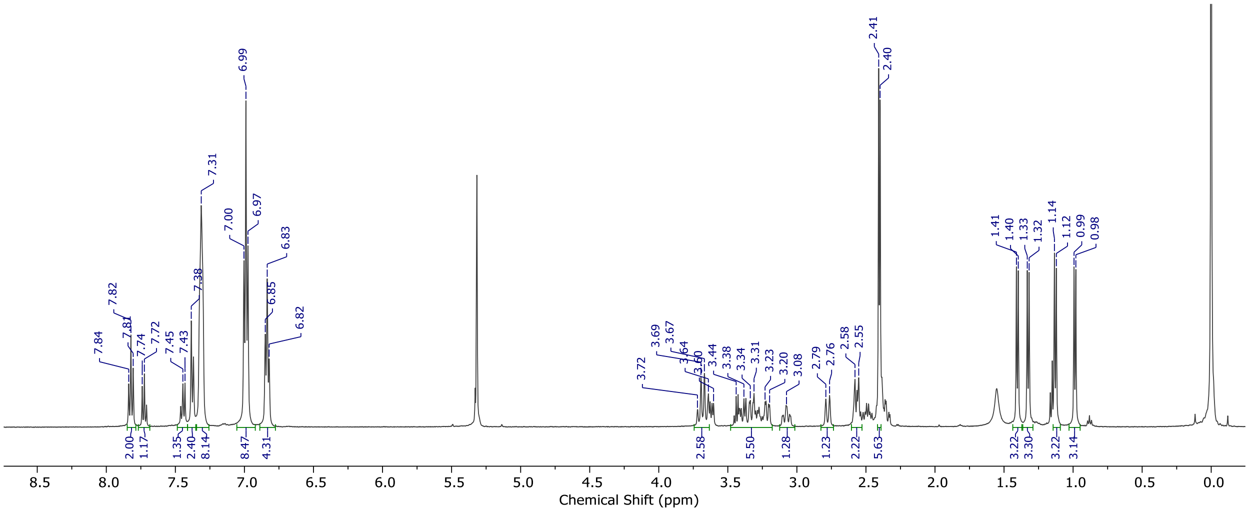

Figure S23 ^{1}H N MR of [**6**FeNO][BPh4] (500 MHz, CD2Cl2, δ): 7.82 (t, 2H), 7.72 (t, 1H), 7.46 – 7.37 (m, 3H), 7.31 (br, 8H), 6.99 (t, 8H), 6.83 (t, 4H), 3.68 (q, 2H), 3.64 – 3.60 (m, 1H), 3.42 – 3.25 (m, 2H), 3.33 (dd, 1H), 3.21 (dd, 1H), 3.08 (td, 1H), 2.78 (d, 1H), 2.57 (d, 1H), 2.57 – 2.46 (m, 2H), 2.41 (s, 3H), 2.40 (s, 3H), 2.34 (dd, 2H), 1.55 (br, 2H), 1.40 (d, 3H), 1.32 (d, 3H), 1.13 (d, 3H), 0.99 (d, 3H).

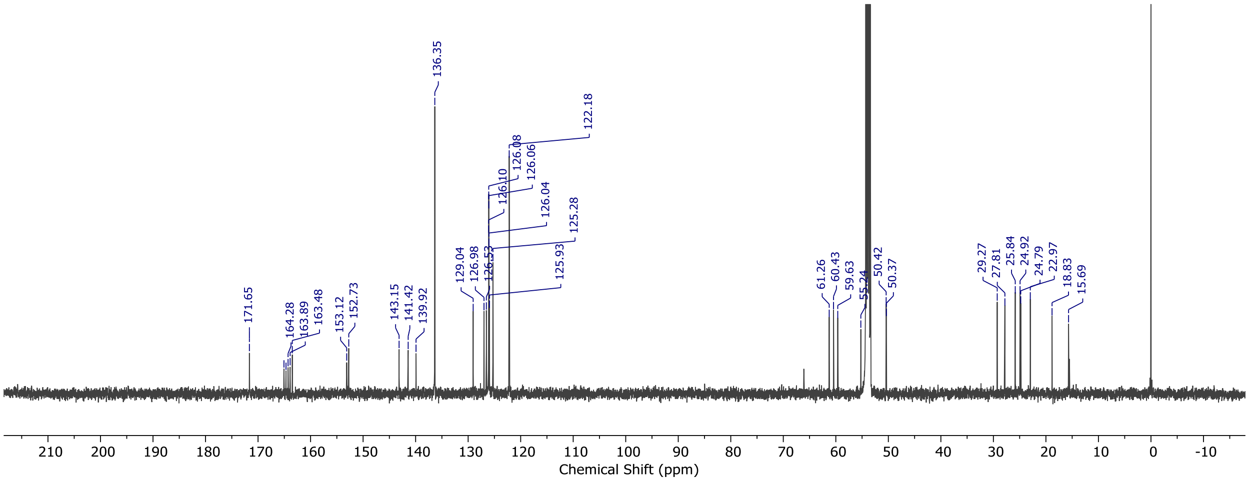

Figure S24 ^{13}C NMR of [**6**FeNO][BPh$_4$] ^{13}C NMR (125 MHz, CD$_2$Cl$_2$, δ): 171.65, 165.07, 164.68, 164.28, 163.89, 163.48, 153.12, 152.73, 143.15, 141.42, 139.92, 136.35, 129.04, 126.98, 126.53, 126.07, 125.93, 125.28, 122.18, 61.26, 60.43, 59.63, 50.42, 29.27, 27.81, 25.84, 24.92, 24.79, 22.97, 18.83, 15.69.

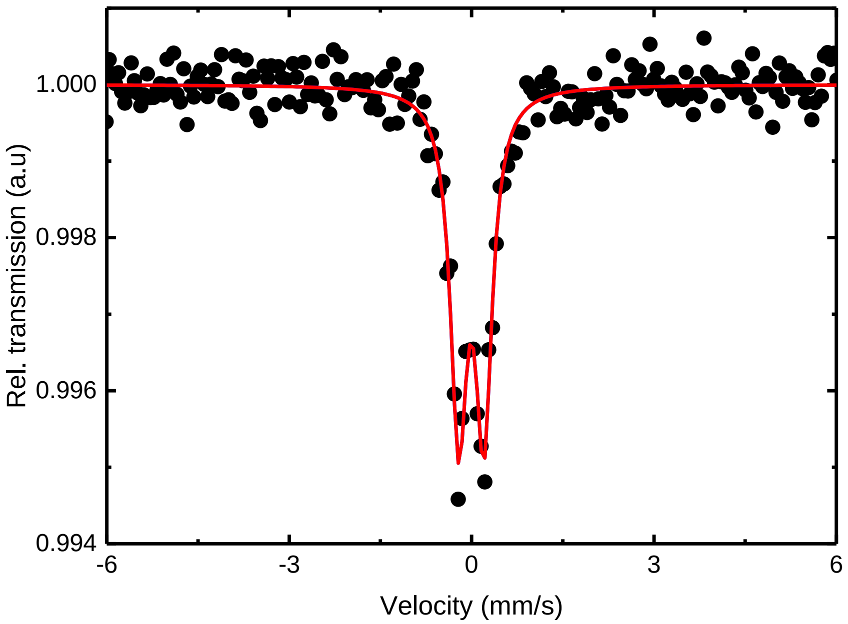

Figure S25 Zero-field Mössbauer Spectrum of [**6**FeNO][BPh4]. Isomershift, δ = 0.095(5) mm/s; quadrupole splitting, ΔEQ = 0.415(9) mm/s; line width, Γ = 0.32(1) mm/s.

Preparation of [6Fe(NO)$_2$][BPh$_4$]

The procedure described for the synthesis of [**7**FeNO][BPh$_4$] was used and replaced **6**Fe(CO)$_2$ with **7**Fe(CO)$_2$. The product was obtained by combining the brown CHCl$_3$ solution separated from the MNIC, followed by precipitation with Et$_2$O (yielded 32%).

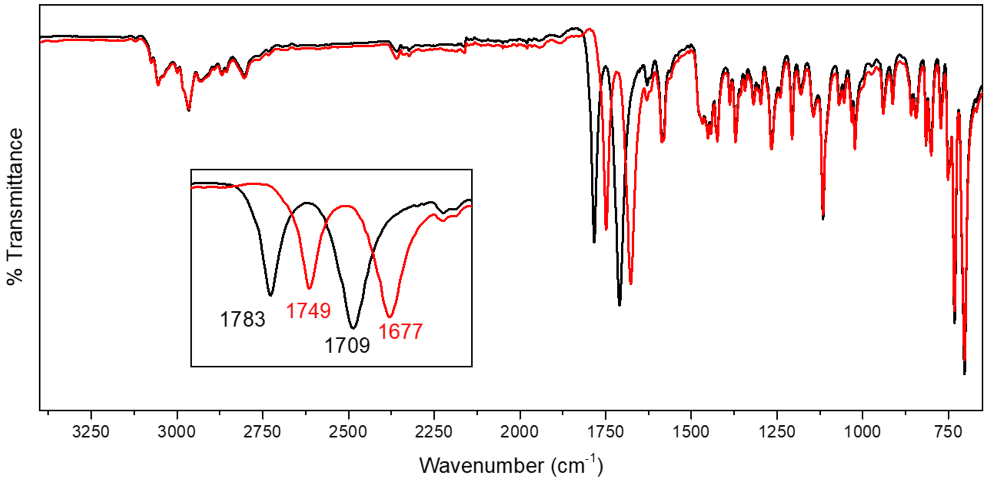

Figure S26 FT-IR (ATR) of [**6**Fe(NO)$_2$][BPh$_4$] and [**6**Fe(^{15}NO)$_2$][BPh$_4$] (black and red, respectively). FTIR (ATR): 1783, 1709 cm^{-1} (^{14}N=O/^{15}N=O); 734, 705 cm^{-1} ($^{-}$BPh$_4$). ν(^{15}N=O) = 1749, 1677 cm^{-1} . Δν(^{14}NO-^{15}NO) = 32 cm^{-1}.

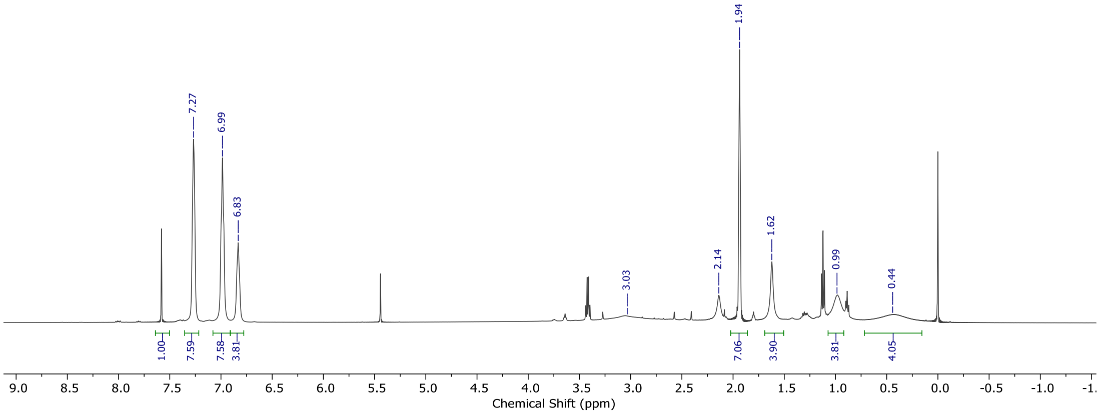

Figure S27 ^{1}H NMR (500 MHz) spectrum of [**6**Fe(NO)$_2$][BPh$_4$] in CD$_3$CN.

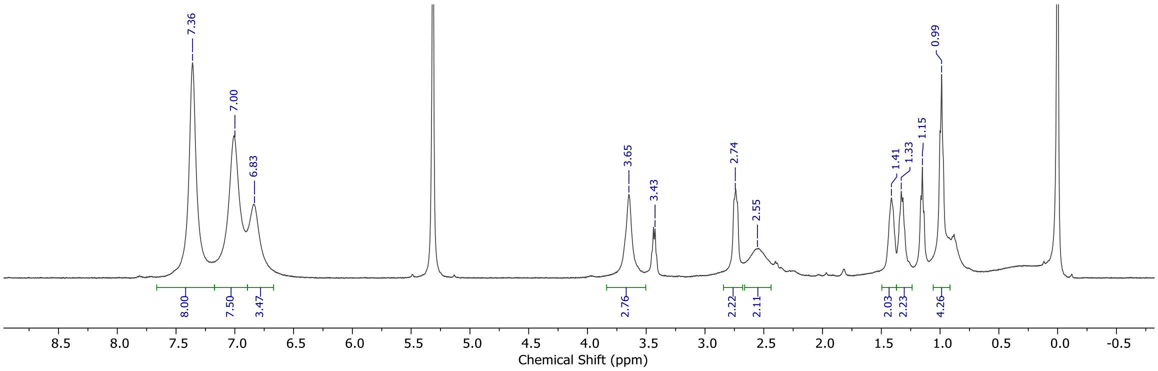

Figure S28 ^{1}H NMR (500 MHz) spectrum of [**6**Fe(NO)$_2$][BPh$_4$] in CD$_2$Cl$_2$.

Electrochemistry.

All electrochemical experiments were performed under N_2 at room temperature in a unless otherwise noted. Data were collected using a Pine WaveNow potentiostat connected to a standard three-electrode cell consisted of a glassy carbon working electrode (A = 0.071 cm^2), a platinum auxiliary electrode and a pseudoreference electrode. The pseudo-reference electrode consisted of a Vycor tip attached to the $Ag^{+/0}$ compartment filled with a fresh 10 mM $AgNO_3$/MeCN solution. A typical sample solution consisted of 1 mM analyte and 0.1 M $TBAPF_6$. After the collection of survey voltammogram in each experiment, crystalline ferrocene (1 equiv. to analyte) was added for reference (. All voltammograms were plotted as measured current vs. applied potentials. All reported potentials were referenced to the $E_{1/2}$ of $Fc^{+/0}$ measured at 100 mV/s, typically without iR compensation.

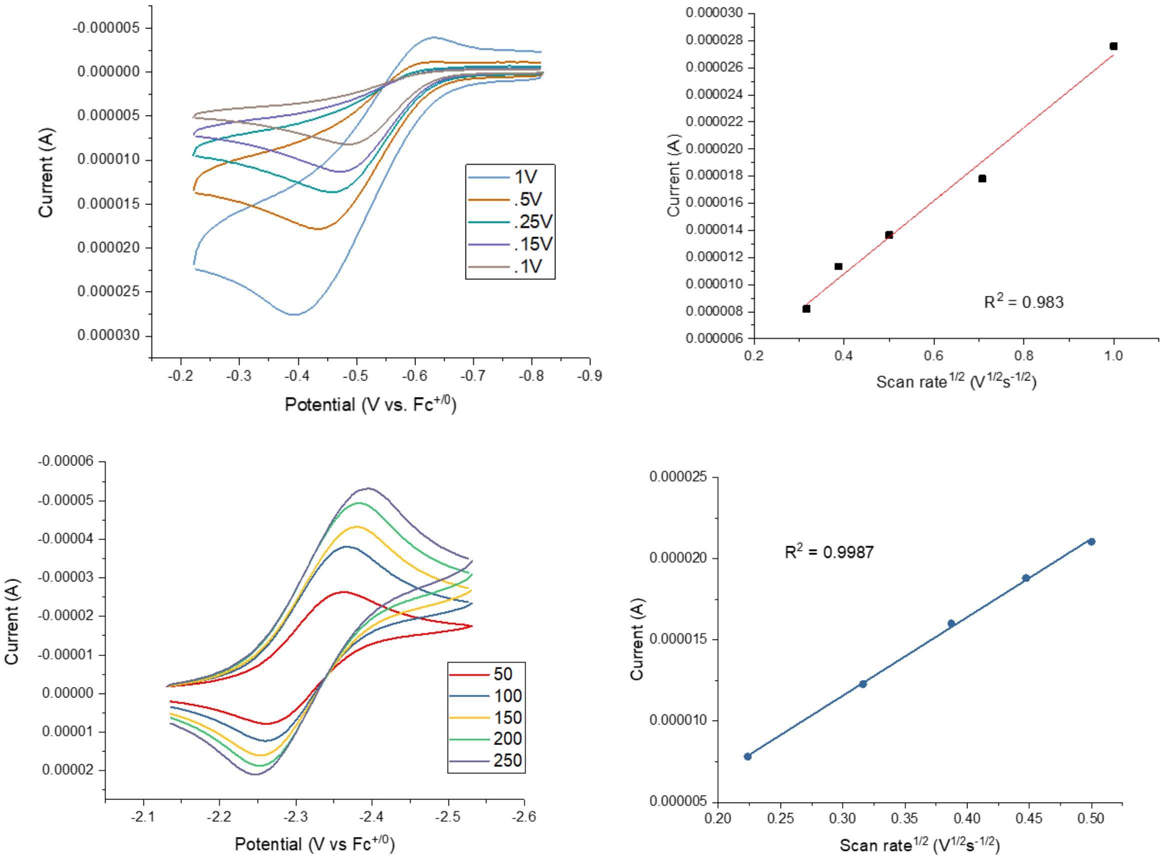

Figure S29 Scan rate dependence reversibility of **7**Fe(CO)$_2$. Top: reversibility of ligand oxidation ($E_{1/2}$ = -0.5245 V; reversibility of this couple is only observed at fast scan rates, indicative of an E_rC_i mechanism, where the reversible electron transfer from the ligand is followed by an immediate chemical step that is irreversible.) Bottom: reversibility of metal-based reduction ($E_{1/2}$ = -2.3132V).

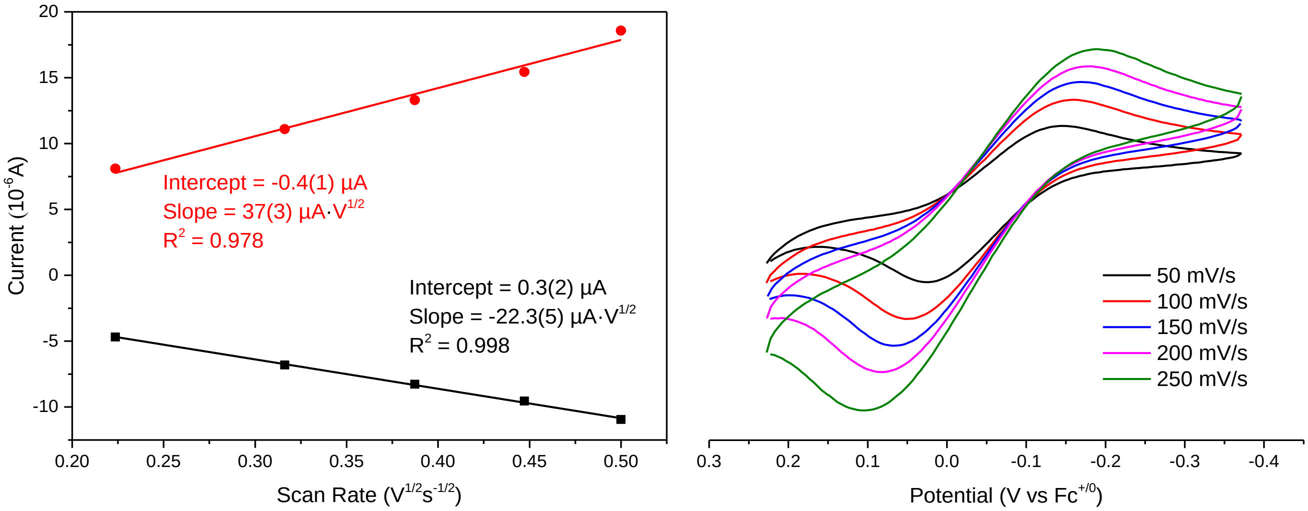

Figure S30 Cyclic voltammograms of [**7**FeNO][BPh_4]; 1 mM sample with 0.1 M $TBAPF_6$ in DCM measured at 50, 100, 150, 200 and 250 mV/s; linear fit of a Randle-Sevcik plot (cathodic and anodic peak current (A) vs scan rate ($V^{1/2}s^{-1/2}$). $E_{1/2}$ = -0.055 V was approximated from the measurement at 100 mV/s.

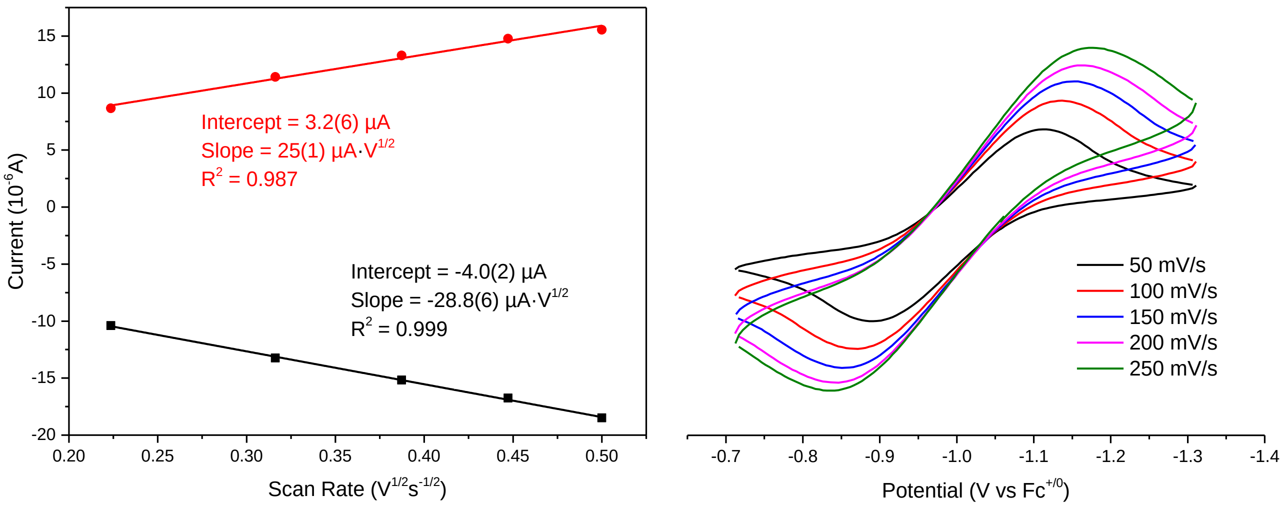

Figure S31 Cyclic voltammograms of [**7**Fe(NO)$_2$][BPh_4]; 1 mM with 0.1 M $TBAPF_6$ in DCM measured at 50, 100, 150, 200 and 250 mV/s; linear fit of a Randle-Sevcik plot (cathodic and anodic peak current (A) vs scan rate ($V^{1/2}s^{-1/2}$). $E_{1/2}$ = -1.00 V.

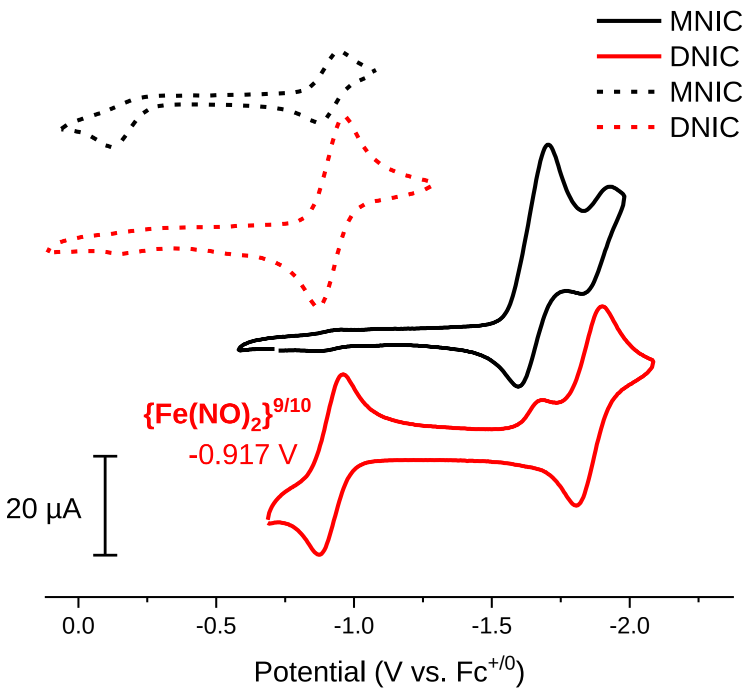

Figure S32 Survey voltammograms of [**7**FeNO][BPh_4] and [**7**$Fe(NO)_2$][BPh_4], labeled as MNIC (black trace) and DNIC (red trace), respectively. The dotted black and dotted red traces show MNIC and DNIC scanned oxidatively up to 0 V. All were recorded under the same conditions (1 mM analyte and 0.1 M $TBAPF_6$ in MeCN). The event at $E_{1/2}$ = -0.917 V vs $Fc^{+/0}$, observable in DNIC only, was assigned the one-electron reduction of $\{Fe(NO)_2\}^9$ to $\{Fe(NO)_2\}^{10}$.

References

(1) *Biological Inorganic Chemistry: Structure and Reactivity*, 1 edition.; Gray, H. B., Stiefel, E. I., Valentine, J. S., Bertini, I., Eds.; University Science Book: Sausalito, Calif, 2006.

(2) Karlin, K. D. Metalloenzymes, Structural Motifs, and Inorganic Models. *Science* **1993**, *261*, 701–708.

(3) Darensbourg, M. Y.; Llobet, A. Preface for Small Molecule Activation: From Biological Principles to Energy Applications. Part 3: Small Molecules Related to (Artificial) Photosynthesis. *Inorg. Chem.* **2016**, *55*, 371–377.

(4) Meyer, F.; Tolman, W. B. Forums on Small-Molecule Activation: From Biological Principles to Energy Applications. *Inorg. Chem.* **2015**, *54*, 5039–5039.

(5) Fowler, D.; Coyle, M.; Skiba, U.; Sutton, M. A.; Cape, J. N.; Reis, S.; Sheppard, L. J.; Jenkins, A.; Grizzetti, B.; Galloway, J. N.; et al. The Global Nitrogen Cycle in the Twenty-First Century. *Philos. Trans. R. Soc. B Biol. Sci.* **2013**, *368*, 20130164–20130164.

(6) Maia, L. B.; Moura, J. J. G. How Biology Handles Nitrite. *Chem. Rev.* **2014**, *114*, 5273–5357.

(7) Lehnert, N.; Peters, J. C. Preface for Small-Molecule Activation: From Biological Principles to Energy Applications. Part 2: Small Molecules Related to the Global Nitrogen Cycle. *Inorg. Chem.* **2015**, *54*, 9229–9233.

(8) Dempsey, J. L.; Winkler, J. R.; Gray, H. B. Proton-Coupled Electron Flow in Protein Redox Machines. *Chem. Rev.* **2010**, *110*, 7024–7039.

(9) Valdez, C. E.; Smith, Q. A.; Nechay, M. R.; Alexandrova, A. N. Mysteries of Metals in Metalloenzymes. *Acc. Chem. Res.* **2014**, *47*, 3110–3117.

(10) Smil, V. *Enriching the Earth*; MIT Press: Cambridge, MA, 2001.

(11) Appling, D. R.; Anthony-Cahill, S. J.; Mathews, C. K. *Biochemistry: Concepts and Connections*, 1 edition.; Pearson, 2015.

(12) Lancaster, K. M.; Roemelt, M.; Ettenhuber, P.; Hu, Y.; Ribbe, M. W.; Neese, F.; Bergmann, U.; DeBeer, S. X-Ray Emission Spectroscopy Evidences a Central Carbon in the Nitrogenase Iron-Molybdenum Cofactor. *Science* **2011**, *334*, 974–977.

(13) Sippel, D.; Rohde, M.; Netzer, J.; Trncik, C.; Gies, J.; Grunau, K.; Djurdjevic, I.; Decamps, L.; Andrade, S. L. A.; Einsle, O. A Bound Reaction Intermediate Sheds Light on the Mechanism of Nitrogenase. *Science* **2018**, *359*, 1484–1489.

(14) Hoffman, B. M.; Lukoyanov, D.; Yang, Z.-Y.; Dean, D. R.; Seefeldt, L. C. Mechanism of Nitrogen Fixation by Nitrogenase: The Next Stage. *Chem. Rev.* **2014**, *114*, 4041–4062.

(15) Structure−Function Relationships of Alternative Nitrogenases - Chemical Reviews (ACS Publications) https://pubs.acs.org/doi/abs/10.1021/cr950057h (accessed Aug 14, 2018).

(16) Metalloproteins Containing Cytochrome, Iron–Sulfur, or Copper Redox Centers - Chemical Reviews (ACS Publications) https://pubs.acs.org/doi/abs/10.1021/cr400479b (accessed Jul 23, 2018).

(17) Shaanan, B. The Iron-Oxygen Bond in Human Oxyhaemoglobin. *Nature* **1982**, *296*, 683–684.

(18) Michel, H.; Behr, J.; Harrenga, A.; Kannt, A. Cytochrome c Oxidase: Structure and Spectroscopy. *Annu. Rev. Biophys. Biomol. Struct.* **1998**, *27*, 329–356.

(19) Meunier, B.; de Visser, S. P.; Shaik, S. Mechanism of Oxidation Reactions Catalyzed by Cytochrome P450 Enzymes. *Chem. Rev.* **2004**, *104*, 3947–3980.

(20) Springer, B. A.; Sligar, S. G.; Olson, J. S.; Phillips, G. N. J. Mechanisms of Ligand Recognition in Myoglobin https://pubs.acs.org/doi/abs/10.1021/cr00027a007 (accessed Aug 14, 2018).

(21) Winkler, J. R.; Gray, H. B. Electron Flow through Metalloproteins. *Chem. Rev.* **2014**, *114*, 3369–3380.

(22) Miller, A.-F. Redox Tuning over Almost 1 V in a Structurally Conserved Active Site: Lessons from Fe-Containing Superoxide Dismutase. *Acc. Chem. Res.* **2008**, *41*, 501–510.

(23) Goodin, D. B.; McRee, D. E. The Asp-His-Iron Triad of Cytochrome c Peroxidase Controls the Reduction Potential Electronic Structure, and Coupling of the Tryptophan Free Radical to the Heme. *Biochemistry* **1993**, *32*, 3313–3324.

(24) Terasaka, E.; Yamada, K.; Wang, P.-H.; Hosokawa, K.; Yamagiwa, R.; Matsumoto, K.; Ishii, S.; Mori, T.; Yagi, K.; Sawai, H.; et al. Dynamics of Nitric Oxide Controlled by Protein Complex in Bacterial System. *Proc. Natl. Acad. Sci.* **2017**, *114*, 9888–9893.

(25) Gordon, Z.; Drummond, M. J.; Matson, E. M.; Bogart, J. A.; Schelter, E. J.; Lord, R. L.; Fout, A. R. Tuning the Fe(II/III) Redox Potential in Nonheme Fe(II)–Hydroxo Complexes through Primary and Secondary Coordination Sphere Modifications. *Inorg. Chem.* **2017**, *56*, 4852–4863.

(26) Morimoto, Y.; Kotani, H.; Park, J.; Lee, Y.-M.; Nam, W.; Fukuzumi, S. Metal Ion-Coupled Electron Transfer of a Nonheme Oxoiron(IV) Complex: Remarkable Enhancement of Electron-Transfer Rates by Sc $^{3+}$. *J. Am. Chem. Soc.* **2011**, *133*, 403–405.

(27) Tsui, E. Y.; Agapie, T. Reduction Potentials of Heterometallic Manganese-Oxido Cubane Complexes Modulated by Redox-Inactive Metals. *Proc. Natl. Acad. Sci.* **2013**, *110*, 10084–10088.

(28) Fukuzumi, S.; Ohkubo, K.; Lee, Y.-M.; Nam, W. Lewis Acid Coupled Electron Transfer of Metal-Oxygen Intermediates. *Chem. - Eur. J.* **2015**, *21*, 17548–17559.

(29) Chirik, P. J.; Wieghardt, K. Radical Ligands Confer Nobility on Base-Metal Catalysts. *Science* **2010**, *327*, 794–795.

(30) Chirik, P. J. Preface: Forum on Redox-Active Ligands. *Inorg. Chem.* **2011**, *50*, 9737–9740.

(31) Caulton, K. G. Systematics and Future Projections Concerning Redox-Noninnocent Amide/Imine Ligands. *Eur. J. Inorg. Chem.* **2012**, *2012*, 435–443.

(32) Delgado, M.; Ziegler, J. M.; Seda, T.; Zakharov, L. N.; Gilbertson, J. D. Pyridinediimine Iron Complexes with Pendant Redox-Inactive Metals Located in the Secondary Coordination Sphere. *Inorg. Chem.* **2016**, *55*, 555–557.

(33) Burns, K. T.; Marks, W. R.; Cheung, P. M.; Seda, T.; Zakharov, L. N.; Gilbertson, J. D. Uncoupled Redox-Inactive Lewis Acids in the Secondary Coordination Sphere Entice Ligand-Based Nitrite Reduction. *Inorg. Chem.* **2018**.

(34) Beer, P. D. Transition Metal and Organic Redox-Active Macrocycles Designed to Electrochemically Recognize Charged and Neutral Guest Species. In *Advances in Inorganic Chemistry*; Sykes, A. G., Ed.; Academic Press, 1992; Vol. 39, pp 79–157.

(35) Reath, A. H.; Ziller, J. W.; Tsay, C.; Ryan, A. J.; Yang, J. Y. Redox Potential and Electronic Structure Effects of Proximal Nonredox Active Cations in Cobalt Schiff Base Complexes. *Inorg. Chem.* **2017**, *56*, 3713–3718.

(36) Cammarota, R. C.; Lu, C. C. Tuning Nickel with Lewis Acidic Group 13 Metalloligands for Catalytic Olefin Hydrogenation. *J. Am. Chem. Soc.* **2015**, *137*, 12486–12489.

(37) Rudd, P. A.; Liu, S.; Gagliardi, L.; Young, V. G.; Lu, C. C. Metal–Alane Adducts with Zero-Valent Nickel, Cobalt, and Iron. *J. Am. Chem. Soc.* **2011**, *133*, 20724–20727.

(38) Kanady, J. S.; Tsui, E. Y.; Day, M. W.; Agapie, T. A Synthetic Model of the Mn3Ca Subsite of the Oxygen-Evolving Complex in Photosystem II. *Science* **2011**, *333*, 733–736.

(39) Kanady, J. S.; Mendoza-Cortes, J. L.; Tsui, E. Y.; Nielsen, R. J.; Goddard, W. A.; Agapie, T. Oxygen Atom Transfer and Oxidative Water Incorporation in Cuboidal Mn $_3$ MO $_n$ Complexes Based on Synthetic, Isotopic Labeling, and Computational Studies. *J. Am. Chem. Soc.* **2013**, *135*, 1073–1082.

(40) Borovik, A. S. Bioinspired Hydrogen Bond Motifs in Ligand Design: The Role of Noncovalent Interactions in Metal Ion Mediated Activation of Dioxygen. *Acc. Chem. Res.* **2005**, *38*, 54–61.

(41) Lu, Y.; Valentine, J. S. Engineering Metal-Binding Sites in Proteins. *Curr. Opin. Struct. Biol.* **1997**, *7*, 495–500.

(42) Yang, J. Y.; Bullock, R. M.; Shaw, W. J.; Twamley, B.; Fraze, K.; DuBois, M. R.; DuBois, D. L. Mechanistic Insights into Catalytic H $_2$ Oxidation by Ni Complexes Containing a Diphosphine Ligand with a Positioned Amine Base. *J. Am. Chem. Soc.* **2009**, *131*, 5935–5945.

(43) Warren, J. J.; Mayer, J. M. Moving Protons and Electrons in Biomimetic Systems. *Biochemistry* **2015**, *54*, 1863–1878.

(44) DuBois, D. L.; Bullock, R. M. Molecular Electrocatalysts for the Oxidation of Hydrogen and the Production of Hydrogen - The Role of Pendant Amines as Proton Relays. *Eur. J. Inorg. Chem.* **2011**, *2011*, 1017–1027.

(45) Burns, K. T.; Marks, W. R.; Cheung, P. M.; Seda, T.; Zakharov, L. N.; Gilbertson, J. D. Uncoupled Redox-Inactive Lewis Acids in the Secondary Coordination Sphere Entice Ligand-Based Nitrite Reduction. *Inorg. Chem.* **2018**.

(46) Roth, J. P.; Lovell, S.; Mayer, J. M. Intrinsic Barriers for Electron and Hydrogen Atom Transfer Reactions of Biomimetic Iron Complexes. *J. Am. Chem. Soc.* **2000**, *122*, 5486–5498.

(47) Warren, J. J.; Mayer, J. M. Hydrogen Atom Transfer Reactions of Iron−Porphyrin−Imidazole Complexes as Models for Histidine-Ligated Heme Reactivity. *J. Am. Chem. Soc.* **2008**, *130*, 2774–2776.

(48) Siek, S.; Dixon, N. A.; Papish, E. T. Electrochemical Reduction of Ttz Copper(II) Complexes in the Presence and Absence of Protons: Processes Relevant to Enzymatic Nitrite Reduction (Ttz R,R′ = Tris(3-R, 5-R′-1, 2, 4-Triazolyl)Borate). *Inorganica Chim. Acta* **2017**, *459*, 80–86.

(49) Kwon, Y. M.; Delgado, M.; Zakharov, L. N.; Seda, T.; Gilbertson, J. D. Nitrite Reduction by a Pyridinediimine Complex with a Proton-Responsive Secondary Coordination Sphere. *Chem. Commun.* **2016**, *52*, 11016–11019.

(50) Delgado, M.; Sommer, S. K.; Swanson, S. P.; Berger, R. F.; Seda, T.; Zakharov, L. N.; Gilbertson, J. D. Probing the Protonation State and the Redox-Active Sites of Pendant Base Iron(II) and Zinc(II) Pyridinediimine Complexes. *Inorg. Chem.* **2015**, *54*, 7239–7248.

(51) Gray, H. B.; Winkler, J. R. The Rise of Radicals in Bioinorganic Chemistry. *Isr. J. Chem.* **2016**, *56*, 640–648.

(52) Li, Y.; Hodak, M.; Bernholc, J. Enzymatic Mechanism of Copper-Containing Nitrite Reductase. *Biochemistry* **2015**, *54*, 1233–1242.

(53) Rorabacher, D. B. Electron Transfer by Copper Centers. *Chem. Rev.* **2004**, *104*, 651–698.

(54) Solomon, E. I.; Heppner, D. E.; Johnston, E. M.; Ginsbach, J. W.; Cirera, J.; Qayyum, M.; Kieber-Emmons, M. T.; Kjaergaard, C. H.; Hadt, R. G.; Tian, L. Copper Active Sites in Biology. *Chem. Rev.* **2014**, *114*, 3659–3853.

(55) Small, B. L.; Brookhart, M.; Bennett, A. M. A. Highly Active Iron and Cobalt Catalysts for the Polymerization of Ethylene. *J. Am. Chem. Soc.* **1998**, *120*, 4049–4050.

(56) Britovsek, G. J. P.; Gibson, V. C.; McTavish, S. J.; Solan, G. A.; White, A. J. P.; Williams, D. J.; Britovsek, G. J. P.; Kimberley, B. S.; Maddox, P. J. Novel Olefin Polymerization Catalysts Based on Iron and Cobalt. *Chem. Commun.* **1998**, *0*, 849–850.

(57) Bianchini, C.; Giambastiani, G.; Guerrero, I. R.; Meli, A.; Passaglia, E.; Gragnoli, T. Simultaneous Polymerization and Schulz−Flory Oligomerization of Ethylene Made Possible by Activation with MAO of a C1-Symmetric [2,6-Bis(Arylimino)Pyridyl]Iron Dichloride Precursor. *Organometallics* **2004**, *23*, 6087–6089.

(58) Bianchini, C.; Mantovani, G.; Meli, A.; Migliacci, F.; Zanobini, F.; Laschi, F.; Sommazzi, A. Oligomerisation of Ethylene to Linear α-Olefins by New Cs- and C1-Symmetric [2,6-Bis(Imino)Pyridyl]Iron and -Cobalt Dichloride Complexes. *Eur. J. Inorg. Chem.* **2003**, *2003*, 1620–1631.

(59) Flisak, Z.; Sun, W.-H. Progression of Diiminopyridines: From Single Application to Catalytic Versatility. *ACS Catal.* **2015**, *5*, 4713–4724.

(60) Alyea, E. C.; Merrell, P. H. Terdentate NNN Donor Ligands Derived from 2,6-Diacetylpyridine. *Synth. React. Inorg. Met.-Org. Chem.* **1974**, *4*, 535–544.

(61) de Bruin, B.; Bill, E.; Bothe, E.; Weyhermüller, T.; Wieghardt, K. Molecular and Electronic Structures of Bis(Pyridine-2,6-Diimine)Metal Complexes $[\mathrm{ML}_2](\mathrm{PF}_6)_n$ (n = 0, 1, 2, 3; M = Mn, Fe, Co, Ni, Cu, Zn) †. *Inorg. Chem.* **2000**, *39*, 2936–2947.

(62) Bowman, A. C.; Milsmann, C.; Hojilla Atienza, C. C.; Lobkovsky, E.; Wieghardt, K.; Chirik, P. J. Synthesis and Molecular and Electronic Structures of Reduced Bis(Imino)Pyridine Cobalt Dinitrogen Complexes: Ligand versus Metal Reduction. *J. Am. Chem. Soc.* **2010**, *132*, 1676–1684.

(63) Bart, S. C.; Lobkovsky, E.; Bill, E.; Chirik, P. J. Synthesis and Hydrogenation of Bis(Imino)Pyridine Iron Imides. *J. Am. Chem. Soc.* **2006**, *128*, 5302–5303.

(64) Tondreau, A. M.; Stieber, S. C. E.; Milsmann, C.; Lobkovsky, E.; Weyhermüller, T.; Semproni, S. P.; Chirik, P. J. Oxidation and Reduction of Bis(Imino)Pyridine Iron Dinitrogen Complexes: Evidence for Formation of a Chelate Trianion. *Inorg. Chem.* **2013**, *52*, 635–646.

(65) Bart, S. C.; Chłopek, K.; Bill, E.; Bouwkamp, M. W.; Lobkovsky, E.; Neese, F.; Wieghardt, K.; Chirik, P. J. Electronic Structure of Bis(Imino)Pyridine Iron Dichloride, Monochloride, and Neutral Ligand Complexes: A Combined Structural, Spectroscopic, and Computational Study. *J. Am. Chem. Soc.* **2006**, *128*, 13901–13912.

(66) Tondreau, A. M.; Milsmann, C.; Lobkovsky, E.; Chirik, P. J. Oxidation and Reduction of Bis(Imino)Pyridine Iron Dicarbonyl Complexes. *Inorg. Chem.* **2011**, *50*, 9888–9895.

(67) Kleigrewe, N.; Steffen, W.; Blömker, T.; Kehr, G.; Fröhlich, R.; Wibbeling, B.; Erker, G.; Wasilke, J.-C.; Wu, G.; Bazan, G. C. Chelate Bis(Imino)Pyridine Cobalt Complexes: Synthesis, Reduction, and Evidence for the Generation of Ethene Polymerization Catalysts by Li^+ Cation Activation. *J. Am. Chem. Soc.* **2005**, *127*, 13955–13968.

(68) Jurca, T.; Dawson, K.; Mallov, I.; Burchell, T.; Yap, G. P. A.; Richeson, D. S. Disproportionation and Radical Formation in the Coordination of “GaI” with Bis(Imino)Pyridines. *Dalton Trans* **2010**, *39*, 1266–1272.

(69) Vande Linde, A. M. Q.; Juntunen, K. L.; Mols, Ole.; Ksebati, M. Bachar.; Ochrymowycz, L. A.; Rorabacher, D. B. Direct Determination of the Self-Exchange Electron-Transfer Rate Constant for a Copper(II/I) Macrocyclic Pentathiaether Complex. *Inorg. Chem.* **1991**, *30*, 5037–5042.

(70) Xie, B.; Elder, T.; Wilson, L. J.; Stanbury, D. M. Internal Reorganization Energies for Copper Redox Couples: The Slow Electron-Transfer Reactions of the $[Cu^{II/I}(Bib)_2]^{2+/+}$ Couple. *Inorg. Chem.* **1999**, *38*, 12–19.

(71) Chaka, G.; Ochrymowycz, L. A.; Rorabacher, D. B. Physical Parameters and Electron-Transfer Kinetics of the Copper(II/I) Complex with the Macrocyclic Sexadentate Ligand $[18]AneS_6$. *Inorg. Chem.* **2005**, *44*, 9105–9111.

(72) Krylova, K.; Kulatilleke, C. P.; Heeg, M. J.; Salhi, C. A.; Ochrymowycz, L. A.; Rorabacher, D. B. A Structural Strategy for Generating Rapid Electron-Transfer Kinetics in Copper(II/I) Systems. *Inorg. Chem.* **1999**, *38*, 4322–4328.

(73) Cheung, P. M.; Berger, R. F.; Zakharov, L. N.; Gilbertson, J. D. Square Planar Cu(I) Stabilized by a Pyridinediimine Ligand. *Chem. Commun.* **2016**, *52*, 4156–4159.

(74) Houser, R. P.; Blackbum, N. J. Structural Characterization of the First Example of a Bis@-Thiolato)Dicopper(II)Complex. Relevance to Proposals for the Electron Transfer Sites in Cyto- Chrome c Oxidase and Nitrous Oxide Reductase. 2.

(75) Kendall, A. J.; Zakharov, L. N.; Gilbertson, J. D. Synthesis and Stabilization of a Monomeric Iron(II) Hydroxo Complex via *Intra* Molecular Hydrogen Bonding in the Secondary Coordination Sphere. *Inorg. Chem.* **2010**, *49*, 8656–8658.

(76) Delgado, M. Probing the Secondary Coordination Sphere of Zn(II) and Fe(II) Pyridinediimine (PDI) Complexes. 142.

(77) Knijnenburg, Q.; Gambarotta, S.; Budzelaar, P. H. M. Ligand-Centred Reactivity in Diiminepyridine Complexes. *Dalton Trans.* **2006**, *0*, 5442–5448.

(78) Enright, D.; Gambarotta, S.; Yap, G. P. A.; Budzelaar, P. H. M. The Ability of the α,A′-Diiminopyridine Ligand System to Accept Negative Charge: Isolation of Paramagnetic and Diamagnetic Trianions. *Angew. Chem. Int. Ed.* **2002**, *41*, 3873–3876.

(79) Britovsek, G. J. P.; Clentsmith, G. K. B.; Gibson, V. C.; Goodgame, D. M. L.; McTavish, S. J.; Pankhurst, Q. A. The Nature of the Active Site in Bis(Imino)Pyridine Iron Ethylene Polymerisation Catalysts. *Catal. Commun.* **2002**, *3*, 207–211.

(80) Addison, A. W.; Rao, T. N.; Reedijk, J.; van Rijn, J.; Verschoor, G. C. Synthesis, Structure, and Spectroscopic Properties of Copper(II) Compounds Containing Nitrogen–Sulphur Donor Ligands; the Crystal and Molecular Structure of Aqua[1,7-Bis(N-Methylbenzimidazol-2′-Yl)-2,6-Dithiaheptane]Copper(II) Perchlorate. *J Chem Soc Dalton Trans* **1984**, No. 7, 1349–1356.

(81) Fielding, L. Determination of Association Constants (Ka) from Solution NMR Data. *Tetrahedron* **2000**, *56*, 6151–6170.

(82) Ford, P. C.; Lorkovic, I. M. Mechanistic Aspects of the Reactions of Nitric Oxide with Transition-Metal Complexes. *Chem. Rev.* **2002**, *102*, 993–1018.

(83) Latimer, W. M. *Oxidation Potentials. Second Edition*; Prentice Hall, 1952.

(84) Bartberger, M. D.; Liu, W.; Ford, E.; Miranda, K. M.; Switzer, C.; Fukuto, J. M.; Farmer, P. J.; Wink, D. A.; Houk, K. N. The Reduction Potential of Nitric Oxide (NO) and Its Importance to NO Biochemistry. *Proc. Natl. Acad. Sci.* **2002**, *99*, 10958–10963.

(85) Delgado, M.; Gilbertson, J. D. Ligand-Based Reduction of Nitrate to Nitric Oxide Utilizing a Proton-Responsive Secondary Coordination Sphere. *Chem Commun* **2017**, *53*, 11249–11252.

(86) Burns, K. T.; Marks, W. R.; Cheung, P. M.; Seda, T.; Zakharov, L. N.; Gilbertson, J. D. Uncoupled Redox-Inactive Lewis Acids in the Secondary Coordination Sphere Entice Ligand-Based Nitrite Reduction. 31.

(87) Enemark, J. H.; Feltham, R. D. Principles of Structure, Bonding, and Reactivity for Metal Nitrosyl Complexes. *Coord. Chem. Rev.* **1974**, *13*, 339–406.

(88) Tsai, M.-L.; Tsou, C.-C.; Liaw, W.-F. Dinitrosyl Iron Complexes (DNICs): From Biomimetic Synthesis and Spectroscopic Characterization toward Unveiling the Biological and Catalytic Roles of DNICs. *Acc. Chem. Res.* **2015**, *48*, 1184–1193.

(89) Ye, S.; Neese, F. The Unusual Electronic Structure of Dinitrosyl Iron Complexes. *J. Am. Chem. Soc.* **2010**, *132*, 3646–3647.

(90) Serres, R. G.; Grapperhaus, C. A.; Bothe, E.; Bill, E.; Weyhermüller, T.; Neese, F.; Wieghardt, K. Structural, Spectroscopic, and Computational Study of an Octahedral, Non-Heme {Fe−NO}6-8 Series: [Fe(NO)(Cyclam-Ac)]2+/+/0. 16.

(91) Wyllie, G. R. A.; Schulz, C. E.; Scheidt, W. R. Five- to Six-Coordination in (Nitrosyl)Iron(II) Porphyrinates: Effects of Binding the Sixth Ligand. *Inorg. Chem.* **2003**, *42*, 5722–5734.

(92) Roncaroli, F.; Videla, M.; Slep, L. D.; Olabe, J. A. New Features in the Redox Coordination Chemistry of Metal Nitrosyls {M–NO+; M–NO; M–NO−(HNO)}. *Coord. Chem. Rev.* **2007**, *251*, 1903–1930.

(93) Dilworth, J. R.; Henderson, R. A.; Dahlstrom, P.; Nicholson, T.; Zubieta, J. A. The Chemistry of the Hydrazido(1–)-Ligand. Preparations and Crystal Structures of [Mo(NHNHCO$_2$Me)(NNCO$_2$Me)(S$_2$CNMe$_2$)$_2$], [Mo(NHNMePh)(NNMePh)(S$_2$CNMe$_2$)$_2$]BPh$_4$, and [ReCl$_2$(NHNHCOPh)(NNHCOPh)(PPh$_3$)$_2$]. Mechanism of Formation of Substituted Hydrazines from [Mo(NNRPh)$_2$(S$_2$CNMe$_2$)$_2$](R = Me or Ph). *J Chem Soc Dalton Trans* **1987**, No. 3, 529–540.

(94) Grönberg, K. L. C.; Henderson, R. A.; Oglieve, K. E. A Unified Mechanism for the Stoichiometric Reduction of H+ and C2H2 by [Fe4S4(SPh)4]3− in MeCN. *J. Chem. Soc. Dalton Trans.* **1998**, No. 18, 3093–3104.

(95) Kaljurand, I.; Kütt, A.; Sooväli, L.; Rodima, T.; Mäemets, V.; Leito, I.; Koppel, I. A. Extension of the Self-Consistent Spectrophotometric Basicity Scale in Acetonitrile to a Full Span of 28 pK_a Units: Unification of Different Basicity Scales. *J. Org. Chem.* **2005**, *70*, 1019–1028.